Chapter 4

The EPIC dual-radiator RICH

This Chapter focuses on Electron-Ion Collider (EIC), designed to be the world-leading facility to explore ~~the~~ QCD. EIC goals are to provide precision 3D imaging of ~~protons~~ and nuclei, solve the proton spin~~-~~puzzle, investigate the quark and gluon confinement, and measure the peculiar correlations of quarks and gluons in ~~the nuclei.~~ The author significantly contributed to the development of the dual-radiator Ring Imaging Cherenkov (dRICH) for the Electron-Proton/Ion Collider Experiment (ePIC) experiment, a key component for identifying the hadrons produced in the collisions. In particular, the author contributed to the studies based on the dRICH prototype performed along several test beams between 2021 and 2023. He developed the analysis software and the simulation framework, characterized the aerogel radiator samples, and was responsible for the tracking system during the data acquisition. The results obtained by the prototype are comparable with the expectation derived from the simulation and satisfy the requirements for the experiment.

4.1 The EPIC experiment at the Electron-Ion Collider

The EIC [37] is the new large-scale accelerator machine, which will be built at Brookhaven National Laboratory (BNL) ~~on~~ Long Island, New York, USA. The EIC will collide high-energy electron beams with high-energy proton and ion beams. The EIC will exploit high-intensity polarized beams to investigate QCD's new frontiers. The main design requirements of the EIC are:

- Beams of various ion species, from proton to uranium;
- Highly polarized beams $\sim 70\%$;

- Variable e+p center-of-mass energies in the range $20 \div 140\,\text{GeV}$;
- High collision electron-ion luminosity $10^{33} \div 10^{34}\,\text{cm}^{-2}\text{s}^{-1}$;
- Up to two general-purpose detectors.

These ~~performances~~ will be accomplished using an electron storage ring with up to 18 GeV beam energy and a hadron storage ring operating at energies 41 GeV and ~~100 to~~ 275 GeV (protons), or 41 GeV and ~~100 to~~ 110 GeV/nucleon (ion). The two beams will collide at a crossing angle of 25 mRad, allowing a quick separation, to bring focusing beam elements close to the interaction point and keep the synchrotron radiation background low. The EIC will replace the Relativistic Heavy Ion Collider (RHIC), the machine at BNL that is in operation until 2025. A scheme of the new accelerator is represented in Figure 4.1.

The first detector will be run by the 2022-born Electron-Proton/Ion Collider Experiment (ePIC) collaboration and located at the collider interaction point IP6. The ePIC collaboration includes 171 institutions from 24 countries and more than 500 participants. According to the scheme in Figure 4.2, ePIC will consist of a barrel-shaped central detector built around a 2 T solenoidal magnet, a far-forward electron detector, and a far-backward hadron spectrometer. These three detectors contribute to cover the whole phase space of the asymmetric lepton-hadron collision. Indeed, the three components of the experiment can see very different particles in terms of both momentum and particle types.

The magnet

The ePIC magnet will be the MAgnet with Renewed COils (MARCO), a 3.5 m long superconductive solenoid measuring 2.84 m of bore diameter at room temperature, providing a 2 T on-axis field directed along the beamline. The MARCO will operate at 4.5 K.

The tracking and vertexing system

The ePIC tracking has to efficiently recognize patterns, provide a low material budget not exceeding $5\%\cancel{X/}X_0$, work inside the magnetic field, satisfy the geometrical constraints imposed by the solenoid in the barrel ~~detector,~~ and disentangle signal ~~and~~ background. The system under development is a concept detector based on silicon and gaseous tracking technologies to ensure satisfactory space resolution, space point coordinates redundancy, and good time resolution. In particular, it will be based on the Monolithic Active Pixel Silicon (MAPS) tracker, providing ~~the~~ spacial resolution less than 5 µm (3 µm for vertex layer), and Multi-Pattern Gas Detectors (MGPDs), that can be implemented as µMEGAS or µRWELL to provide ~~the~~ redundancy and a time resolution better than 10 ns.

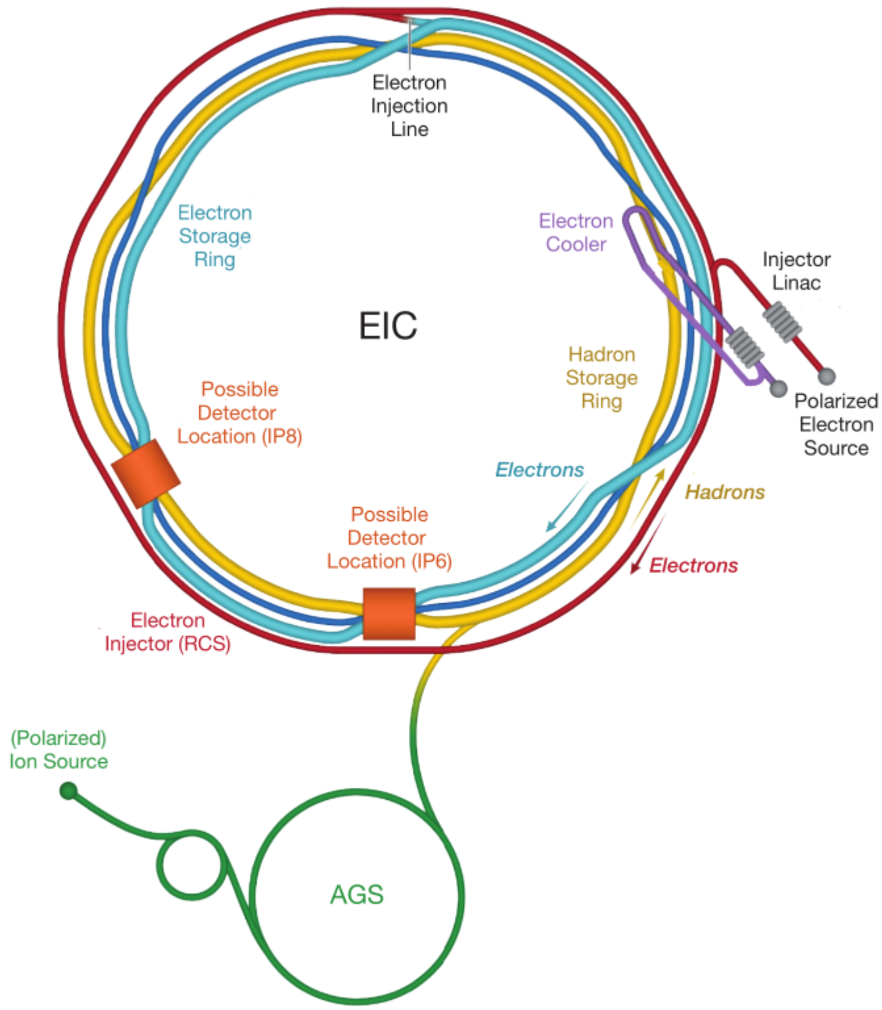

Figure 4.1: Scheme of the Electron-Ion Collider. The ePIC experiment will be located at the interaction point IP6.

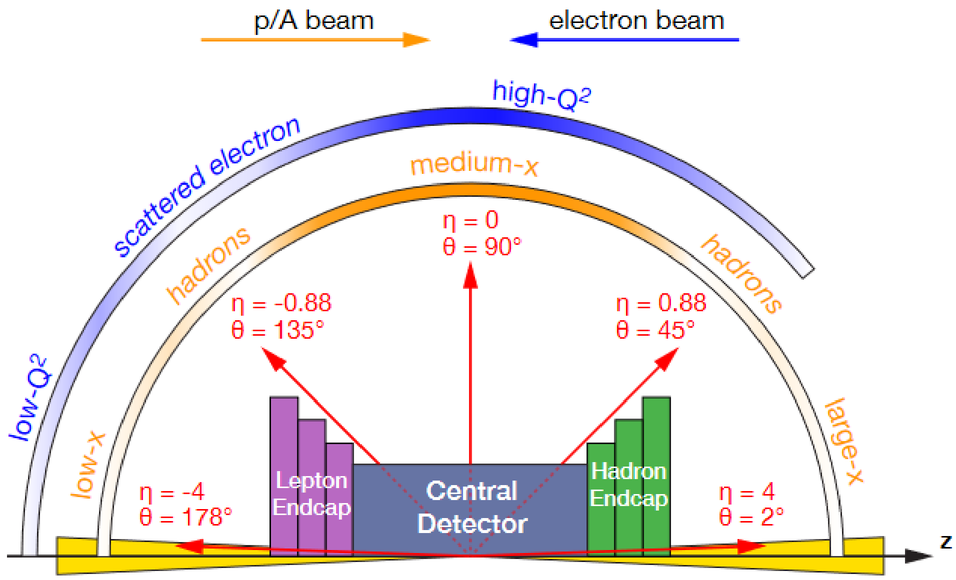

Figure 4.2: Scheme of the ePIC detector

The calorimetry system

The ePIC calorimetry system ~~had~~ to measure the particle's energy, provide continuous acceptance over the entire rapidity spectrum, be insensitive to the magnetic field, and operate up to the maximum luminosity in the expected background conditions. It must also contribute to distinguishing electrons and photons and measure the particle's angle and position.

The Barrel Electromagnetic Calorimeter (bECAL) requires an energy resolution ~~lower~~ than $\frac{7\%}{\sqrt{E}} \oplus 1\%$ and a fine granularity for good $\gamma - \pi^0$ separation. It has to measure energy ~~low~~ to 100 MeV and up to 10 GeV. These requirements must be achieved in a minimal space due to the geometrical constraints imposed by the solenoid. The detector will be a sampling calorimeter based on 6 layers of Astropix sensors ~~alternate by~~ 5 layers of lead and scintillating fibers readout by SiPM on both side. The Astropix are SiPM developed for the Amego-X NASA missions and are used for electromagnetic shower imaging. The scintillating fibers are used to profile the longitudinal dimension. The design allows to obtain a deep by still very compact calorimeter ($\sim 17\cancel{X/}X_0$ in 40 cm), an excellent energy resolution ($\frac{5.2\%}{\sqrt{E}} + 1\%$), an unrivaled low-energy electron-pion separation by combining energy measurement and imaging, and an exceptional position resolution. Moreover, the bECAL is deep enough to serve as the inner layer of the hadronic calorimeter.

The Barrel Hadronic Calorimeter (bHCAL) aims to precisely reconstruct the jet energy, provide a secondary determination of scattered electron kinematics, and help in muon identification. Moreover, it will also serve as part of the solenoid flux return. The bHCAL will be realized by refurbishing the sPHENIX outer HCAL, a cylinder of 1.9 m inner and 2.6 m outer radius, 6.5 m long, made by 32 sectors including 48 towers of scintillators.

The Backward Electromagnetic Calorimeter (eECAL) plays a crucial role in almost every physics channel because it is responsible for detecting and measuring the kinematic of the scattered electron in the backward region, with rapidity $-3.5 < \eta < -1$. In particular, its goals are to separate electrons and pions, to provide a suitable resolution for electron detection at large $|\eta|$, to measure photons with good resolution, and to separate the 2γ from π^0 at high energy. The requirements for this detector are:

- Energy resolution of $\frac{2\%}{\sqrt{E}} + (1 \div 3)\%$;
- Pion suppression $1 : 10^4$;
- Minimum detection energy 50 MeV.

The eECAL ~~will comprise~~ ~ 2850 $20 \times 20 \times 20\,\mathrm{cm}^3$ PWO crystals that fill a disk around the beamline. Each crystal will be read by 16 SiPMs connected to the front-end electronics. One of the most critical points regards the cooling system; thermal studies are ongoing to find the best solutions for efficiently cooling the system.

The Backward Hadronic Calorimeter (eHCAL) shall provide the functionality of a tail catcher for the electromagnetic calorimeter ~~in~~ electron identification and for the jet kinematics measurement at small x_B. The detector is made by ten alternating layers of 4 cm-thick stainless steel and 4 mm-thick plastic scintillator Kuraray SCSN-81. The scintillator's light will be extracted by 0.83 mm wavelength shifter fibers and detected by SiPMs. The front-end electronics will be selected in common with the other calorimetry systems.

The Forward Electromagnetic Calorimeter (hECAL) shall cover the pseudo-rapidity range $\sim 1 < \eta < 4$, achieve an energy resolution of $\frac{10\% \div 12\%}{\sqrt{E}} + 2\%$, provide a good π^0/γ separation up to 50 GeV, and ~~contributing~~ to the jet reconstruction. Moreover, it has to work in a magnetic region with expected neutron fluxes up to $10^{12}\,\mathrm{n/cm}^2$. It will be a sampling calorimeter of tungsten and scintillating fibers.

The Forward Hadronic Calorimeter (hHCAL) shall measure the energy with a resolution of $\frac{50\%}{\sqrt{E}} + 10\%$, with a minimum detected energy of 500 MeV. A high-granularity sampling calorimeter will cover the whole azimuthal angle by alternating small scintillator tiles and absorbing layers.

Particle Identification System

The Particle Identification (PID) system plays a key role in QCD studies as provide flavor sensitivity, particularly for SIDIS. A plot reporting the phase space that needs to be covered by each PID subsystem is shown in Figure 4.3.

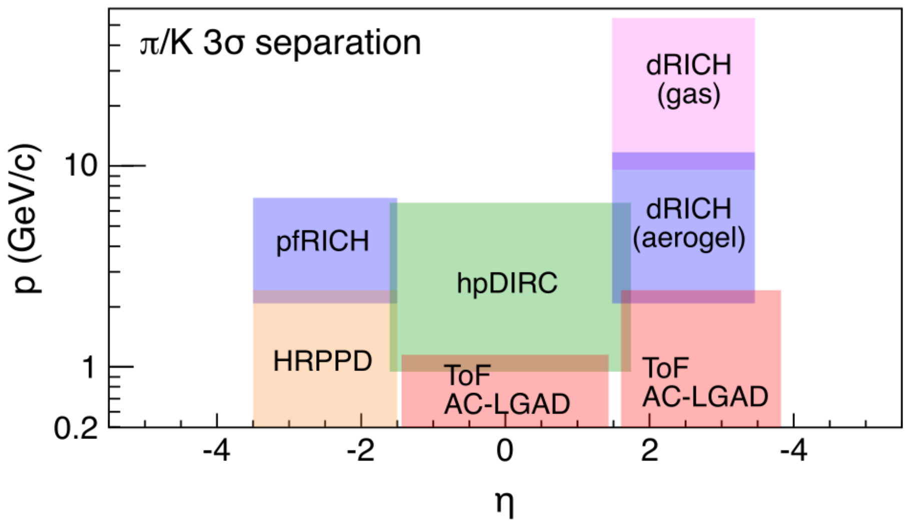

Figure 4.3: Phase space that needs to be covered by each PID subsystem.

In the backward direction, the proximity-focusing RICH (pfRICH) will provide a 3σ separation between π and K up to 7 GeV. Moreover, using the High Rate Picosecond Photo-Detector, the pfRICH will provide a 20 ps-resolution time measurement for a time-of-flight analysis and a spatial resolution of ~ 1 mm. The TOF will provide 3σ separation of low~~er~~ momentum pion and kaon in the barrel ($-1.4 < \eta < 1.4$, $0.2 < p < 1.2$ GeV~~)~~ and in the forward endcap ($-1.74 < \eta < 3.83$, $0.2 < p < 2.3$ GeV~~)~~.

The high~~er~~ momentum hadrons will be detected in the barrel by the high-performance Detection of Internally Reflected Cherenkov light (hpDIRC), a fast-focusing DIRC using a high-resolution 3D reconstruction. It will be made of 120 bars of radiator producing Cherenkov light over a focusing lens, ~~and then the photons will pass through~~ an expansion volume, hitting the photo-detector. It will provide a 3σ separation for π/K up to 6 GeV and for e/π up to 1.2 GeV.

This work focuses on ~~designing~~ the dual-radiator Ring Imaging Cherenkov (dRICH), a compact and cost-effective solution for broad momentum coverage at forward rapidity essential for SIDIS physics. It will interpolate the measurements of the Cherenkov angles of photons produced by relativistic particles crossing two different radiators to identify charged hadrons ~~passing through the detector~~. The dual-radiator unconventional design is due to ~~the~~ most intriguing challenge ~~for~~ this detector: to identify charged hadrons in the extended momentum range between 3 and 50 GeV. Indeed, this momentum range ~~crosses~~ the few-GeV momentum region where ~~the radiator is usually the aerogel~~ and the high-momentum region where the gas radiator should be used. The dRICH will identify particles in the pseudo-rapidity

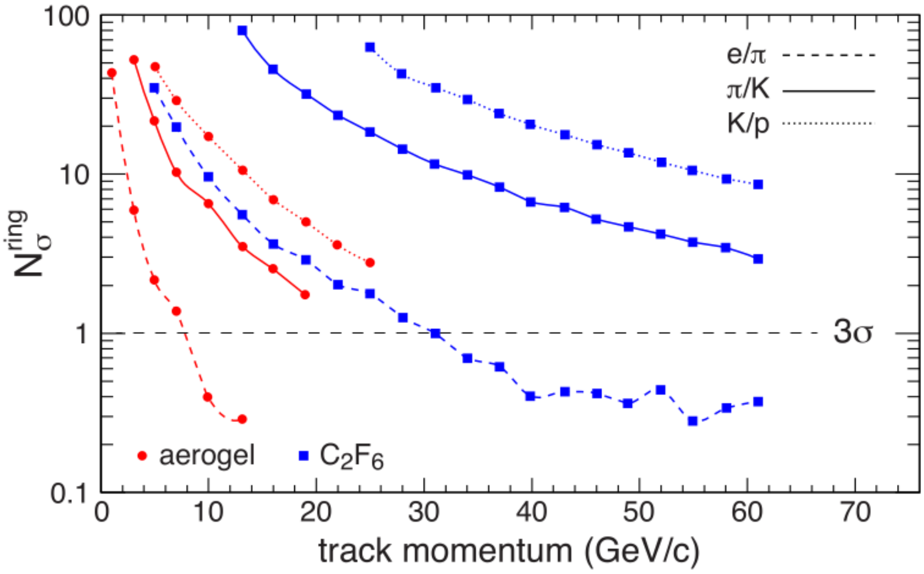

Figure 4.4: Expected separation achievable from the dRICH for a variety of particle species. Combining the aerogel and gas information provides uninterrupted PID across the full range.

range $1.5 < \eta < 3.5$ and help identify electrons with momenta lower than 15 GeV~~,~~ This detector should cope with the ~~specific~~ challenge of ~~working~~ in a high magnetic field, in the order of 1 T, so the magnetic-insensitive Silicon Photomultipliers (SiPMs) sensors are expected to be used. The usage of SiPM introduces a different ~~problem~~ related to the radiation damage that will occur on the sensors, increasing their dark count: a study on the recovery of the sensors via~~-~~annealing was performed and described later in this work. The expected performance of the detector is described in Reference [37] and is reported in Figure 4.4. The rest of the Chapter will describe the ongoing studies on the ~~recovery~~ of SiPM radiation damage and the performances achieved with the ~~prototype of dRICH~~ assembled in Ferrara in 2021.

4.2 The recovery of SiPM radiation damage via annealing

It is expected that during the lifetime of the ePIC experiment, the photosensors of the dRICH will receive radiation in the order of $10^{11}\,\mathrm{n_{eq}/cm^2}$, which will dramatically affect the Dark Count Rate (DCR), increasing it over the acceptable rate of $\sim$ ~~100~~ kHz.~~-~~Several options are available to maintain the DCR to an acceptable level, namely by reducing the SiPM operating temperature (cooling), using the timing information of high-precision Time-to-Digital converter electronics (gating), and recovering the radiation damage

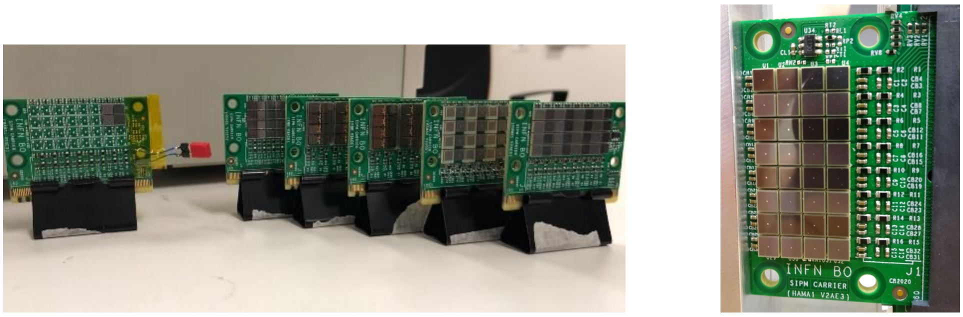

Figure 4.5: On the left, picture of the boards used for irradiation and annealing campaign. On the right is a close view of one board of SiPM. Each board hosts ~~4, 24, or~~ 32 sensors of $3 \times 3\,\mathrm{mm}^2$ area.

with high-temperature annealing cycles (curing) [29]. ~~The~~ cooling and gating procedures are well known and will be used for the dRICH; ~~the~~ curing via annealing has been the subject of dedicated tests since 2021 and has provided positive indications that confirmed the possibility of using it for the final detector [44]. The following SiPM sensors have been studied:

- Hamamatsu S13360-3050VS and S13360-3025VS;
- Hamamatsu S14160-3050HP and S14160-3015PS;
- Fondazione Bruno Kessler (FBK) NUV-HD-CHK and NU-HD-RH prototype;
- Onsemi MICROFJ-30035.

The SiPM sensors have been irradiated on several occasions between 2021 and 2023 in the experimental room of the Trento Proton Therapy facility; this was done with 140 MeV protons produced in a large and uniform irradiation field [8]. The NIEL-scaling hypothesis is used to normalize the proton fluence to the corresponding 1-MeV neutron equivalent [53]. A dedicated collimator system was designed to deliver the uniform irradiation field in a 3 mm wide slit such that, thanks to a precision micrometric translation system, a single column of sensors (6 or 8 SiPM) in a matrix is irradiated at a given time.

Two pictures of the custom boards are shown in Figure 4.5. For each board, three different columns have been exposed at three different levels of irradiation: 10^9, 10^{10}, and 10^{11} $\mathrm{n_{eq}}$. The fourth column was used to control the background neutrons generated by the scattering system and the collimators. Background neutrons received by each board are estimated to correspond to $\sim 2 \div 3 \times 10^8$ $\mathrm{n_{eq}}$. The sensors were characterized in a climate chamber, which provides a stable room temperature of $-30\,^\circ\mathrm{C}$ to control the background DCR. The characterization station is shown in Figure 4.6.

The effect of the irradiation is represented in Figure 4.7, which shows the increase of the dark current and DCR of the SiPM as a function of the

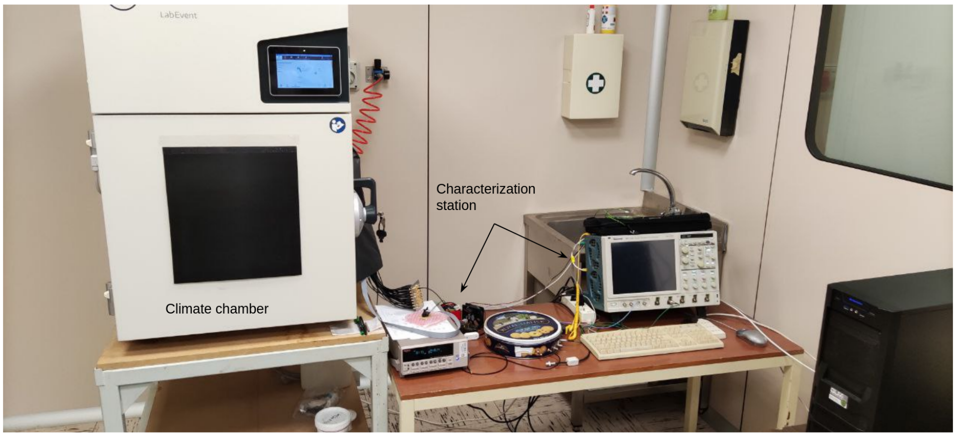

Figure 4.6: The climate chamber and the characterization station used to test the SiPMs in the clean room at INFN Ferrara.

radiation dose. There is a linear increase of current with respect to the dose. The first annealing test was performed using an oven, which is shown in Figure 4.8, and with a staged temperature increase, carrying out various sensor characterizations between each phase of $\sim 50\,\mathrm{h}$ annealing time. The results of these measurements are reported in Figure 4.9, which shows the value of the DCR during this long annealing period compared with the results of Reference [29]. The SiPMs tested in Ferrara showed the same behavior as the reference results, ~~decreasing a~~ factor ~ 20 during the annealing. The systematic comparison of the annealing effect on different sensors is shown in Figure 4.10. It can be noted that the Hamamatsu S13360-3050VS ~~had~~ the lowest DCR before the irradiation and before and after the annealing, which makes it the most promising candidate to be used for the dRICH detector.

After the start of ePIC operation, removing the sensors from the detector for the ~~needed~~ annealing cycles in the oven will be very complex. So, preliminary tests of online in-situ annealing made directly polarizing the SiPM are being performed. The online procedure consists of cycles of 30 min at high temperature (up to 175 °C) each time the sensor received ~~a~~ dose of $2 \times 10^8\,\mathrm{n_{eq}}$. The sensor's temperature should not overcome the value of 180 °C, which is the operating limit ~~of~~ the entrance window protective layer, and was kept under control using a thermal camera, as shown in Figure 4.11a. The comparison between the oven and the online annealing is reported in Figure 4.11b and shows that the online annealing permits a rapid reduction of the DCR by one order of magnitude. The oven annealing performance is better by a factor of 2, but the online procedure has several advantages:

- it is ~ 100 times faster;
- it can be done in-situ, without removing the sensor from the detector;

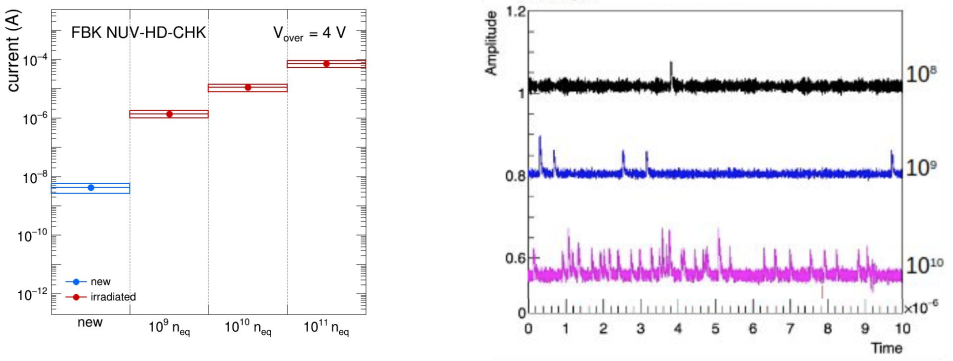

(a) Dark current of a SiPM as a function of the irradiation dose received. It increases linearly with the dose.

(b) Snapshot of the signal of SiPMs which received a different dose of radiation. Each spike corresponds to at least one photo-electron contributing to the dark count. Clearly, increasing the dose leads to larger DCR.

Figure 4.7: Effects of the irradiation on dark current and DCR.

- it can be repeated many times.

Consequently, the final design of the dRICH detector will probably account for several online annealing phases and, at most, ~~one big~~ maintenance operation when sensors are removed for long annealing in the oven.

4.3 The dual-radiator RICH prototype

A prototype [46] of the dRICH detector was built in Ferrara in the summer of 2021, aiming to serve several test beams in the following years. On a lower scale, it reproduces the expected behavior of the entire dRICH detector. It was used to test the hadron separation capabilities that can be achieved. This section identifies the prototype using the acronym dRICH.

4.3.1 Design

A scheme of the prototype is reported in Figure 4.12. A charged particle crossing the prototype from left to right starts passing through the aerogel ($n \simeq 1.02$), producing a Cherenkov-photon cone with an aperture of about $11\,^\circ$. The photons are reflected by a first spherical mirror and focused on the photon detector array. Then, the particle passes through the gas ($n \simeq 1.00085$), which fills the detector volume and produces a Cherenkov-photon cone with an aperture of about $2\,^\circ$. The first mirror has a central hole to allow the photons produced at small angles in the gas to fly towards a second spherical mirror and be focused back on the same photon detector array. The information from the two imaged Cherenkov rings, combined with the beam momentum

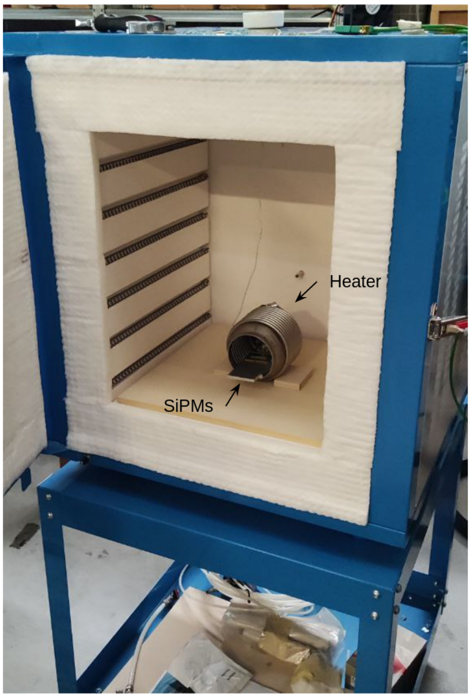

Figure 4.8: The oven used to perform the first annealing in the laboratory of INFN Ferrara.

and particle tagging provided by the beam instrumentation, is used to study the dRICH identification of pions, kaons, and protons in the momentum range from 3 Ge~~V~~ up to 50 Ge~~V~~.

Mechanical structure

The dRICH is 1.3 m long and is composed of two sections: a 50 cm long cylinder with a 50 cm diameter and a 80 cm long extension with a 25 cm diameter. This volume, called the "gas chamber", is filled with the C_2F_6 radiator gas. It has to bear under-pressurization (vacuum), allowing efficient exchange between air and the gaseous radiator, and preserve light tightness, allowing the single-photon operation mode of photo-sensors. Moreover, it includes the mechanics for regulating the angle and position of the mirrors along the detector axis. The radius of curvature of each mirror was designed to collect the light produced over the full radiator length and focus it onto the detector surface. The mechanical support of each mirror can be pre-aligned using three different screws and, without opening the detector, can be moved along the detector axis using a step motor to finely regulate the focus position. A series of pictures of the dRICH components is shown in Figure 4.13.

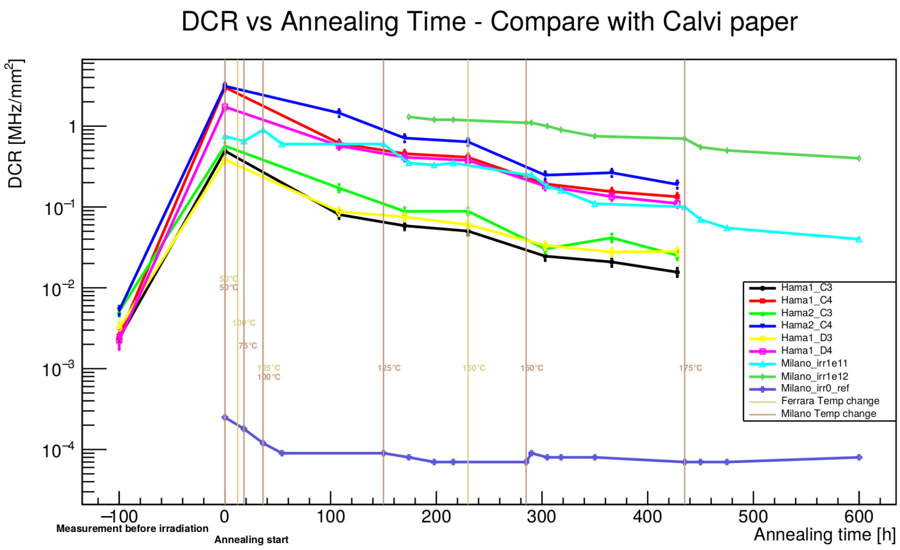

Figure 4.9: Results of the first annealing test using the Ferrara oven and characterization test. The results are compared with Reference [29]. In the legend, “Hama” indicates one of the SiPM by Hamamatsu tested by the author, “C” and “D” identify the ~~raw~~ of the board ~~and then~~ the size of the sipm pixel, “3” and “4” identify the column of the board ~~and then~~ the radiation dose received of 10^{10} or 10^{11} respectively. The “Milano” identifies the curves taken from the Reference paper for different doses of irradiation. The vertical lines show the time ~~of changing temperature~~ and the value of the temperature itself. The points conventionally placed at -100 h represent the DCR before the irradiation at Trento.

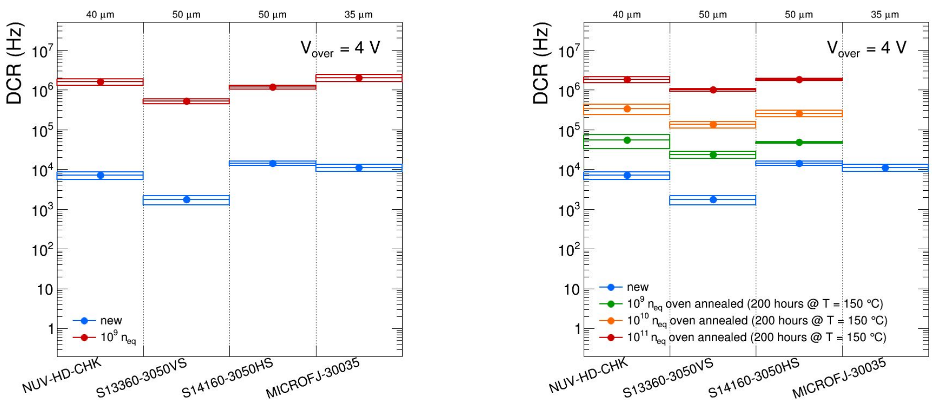

(a) Dark count rate measured for different sensors when they were new and before the annealing).

(b) Dark count rate measured for different sensors and different irradiation dose after 200 h of annealing at 150 °C.

Figure 4.10: Results of irradiation and annealing on different sensors.

(a) Picture of the thermal camera measuring the directly polarized SiPM. The sensor can reach more than 175 °C, but has not to overcome the value of 180 °C.

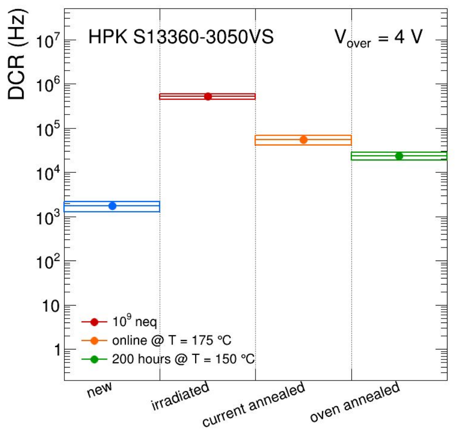

(b) Comparison of the dark count rate measured for the same ~~sensor~~ kind of sensor applying ~~the~~ online ("current") or ~~the~~ oven annealing.

Figure 4.11: Temperature control during the online annealing and results of the annealing performed through the direct polarization of the sensors.

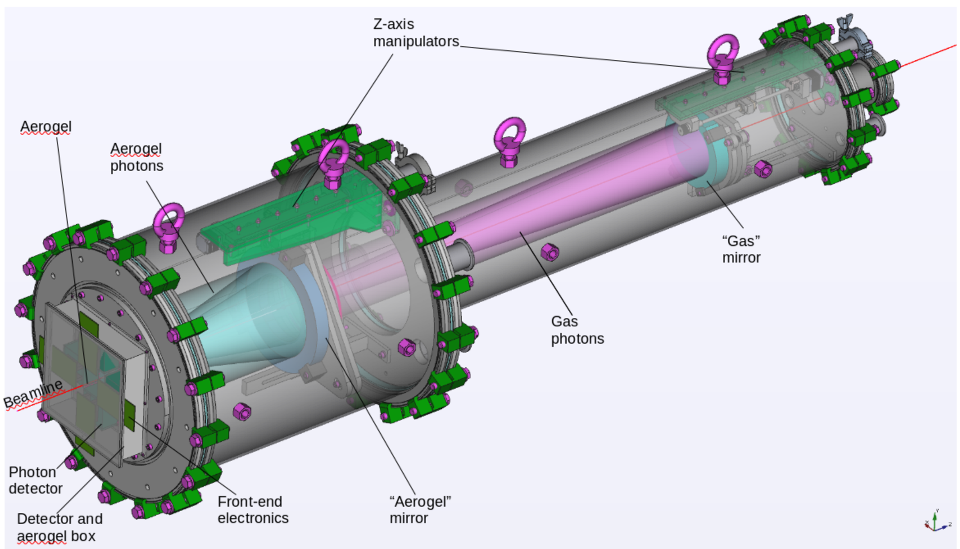

Figure 4.12: dRICH prototype scheme.

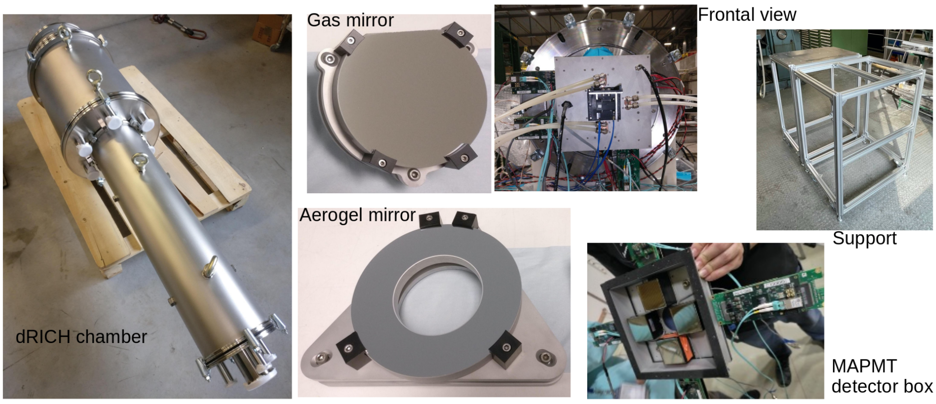

Figure 4.13: Collection of pictures of the prototype components

Detector box

In front of the prototype is the detector box, which hosts the photosensors with their sensitive faces pointed forward and separated from the gas volume by a 3-mm-thick acrylic window. For the prototype, three different kinds of detector boxes were used:

- The MAPMT box hosts four Multi-Anode Photomultiplier Tubes Hamamatsu H12700 (the same as the CLAS12 RICH), set as reference detectors to study the prototype's performance.
- The MPPC box hosts three Multi-Pixel Photon Counters, matrices of SiPMs used during the first test beams as preliminary detectors to study the silicon-based sensors and their cooling system.
- The SiPM box hosts matrices of various Silicon Photomultipliers (undergoing irradiation and annealing cycles) to evaluate the most suitable sensor for the EIC dRICH detector.

The detector boxes are represented in Figure 4.14. The data of the MAPMT and MPPC detector boxes are acquired using the Multi-Anode ReadOut Chip (MAROC) as done for the CLAS12 RICH. Instead, for the SiPM detector box, a streaming readout system based on A Low Power Chip for Optical Sensor Readout (ALCOR) was tested. Initially, the SiPM box was designed to host four small custom matrices used to study the annealing procedure. In the last version, it was modified to host up to 8 photon detection units for a total of 2048 readout channels, made following the current design of the dRICH detector and covering almost the entire ring.

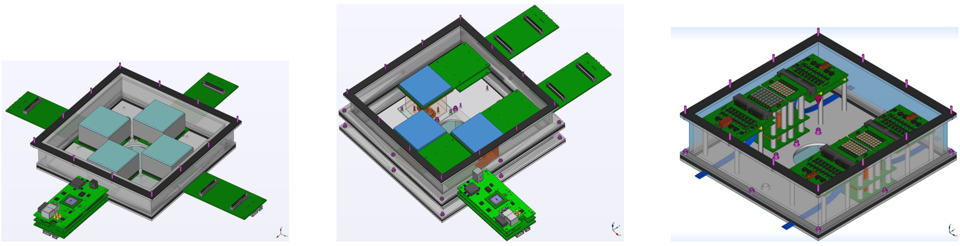

(a) MAPMT detector box. **(b)** MPPC detector box. **(c)** SiPM detector box.

Figure 4.14: Drawing of the three detector boxes.

Aerogel box

The aerogel box completes the mechanical structure. It is a 3D-printed black box containing the aerogel radiator placed upstream of the detector box on the beamline. Black rubber is used to seal the aerogel box to the detector box, preventing light leaks and creating a single volume filled with nitrogen to avoid moisture. The box permits operation in the ePIC configuration with a 4-cm-thick layer of aerogel, but also to test other configurations with 2-cm or 6-cm-thick layers of aerogel.

Radiators

The nominal radiators are the C_2F_6 gas and the aerogel, with refractive index $\simeq 1.00085$ and $\simeq 1.02$, respectively. They present different challenges:

- C_2F_6 is a greenhouse gas, so its use is critical from the point of view of respecting the environment. For the prototype, the relatively small volume allows the use of a simplified recovering system. For the final detector, dedicated special recovery systems are foreseen. Solutions based on the use of pressurized noble gases or alternative gas mixtures are also being studied.

- Silica aerogel is a fragile material and not easy to handle, but in the group working on the dRICH, there is enough experience. The main issue regards the aerogel manufacturer. One of the most commonly used, the Budker and Boreskov Institute of Nuclear Physics (Russia); delivered the aerogel for the CLAS12, LHCb, HERMES and AMS-02 experiments. The invasion of Ukraine introduced insurmountable complications in dealing with this manufacturer. At the moment of writing this document, the candidate supplier is Aerogel Factory Co. [48], a new producer that emerged in 2021 as a spin-off of the Belle-II aerogel development at Chiba University, Japan. They declare the capability of producing aerogel in a wide range of refractive index, from 1.003 to 1.18, and are able to realize samples of good optical quality, which makes them a credible option for producing dRICH aerogel. Because there are different methods to produce aerogel, its properties can be very different, even slightly changing the refractive index. This makes necessary to conduct careful tests before deciding on the producer and take care to characterize each optical property.

This thesis deals with the Cherenkov angle resolution achieved with gas and aerogel radiators, but more attention is paid to aerogel because the author was mainly involved in its study. To evaluate the aerogel produced by the Aerogel Factory Co., several samples were characterized in the laboratory of INFN Ferrara group and tested using the prototype at CERN.

4.3.2 Aerogel characterization

Transmittance analysis

Table 4.1 reports a recap of the aerogel tiles studied. A Perkin Elmer UV/VIS spectrophotometer Lambda 650S was used to characterize the aerogel. The spectrophotometer measures the transmittance of the sample as a function of the photon wavelength. The transmittance was analyzed using the extended Hunt formula [41]

$$T(\lambda) = e^{-\frac{t}{\Lambda_T}} = e^{-t\left(\frac{1}{\Lambda_A}+\frac{1}{\Lambda_S}\right)} = Ae^{-\frac{Bt}{\lambda^8}}e^{-\frac{Ct}{\lambda^4}} \tag{4.1}$$

where T is the transmittance, λ is the wavelength of the light, $\Lambda_{A,S}$ are respectively the Absorpion and Scattering length, and A, B, and C are ~~the~~ parameters~~.~~ An example of fitted transmittance is reported in Figure 4.15. From this formula, it is possible to obtain the values of absorption and scattering length

$$\Lambda_S = \frac{\lambda^4}{C} \tag{4.2}$$

and

$$\Lambda_A = \frac{\lambda^8 t}{Bt - \lambda \cdot \ln A} \tag{4.3}$$

The total transmission length is defined as

$$\frac{1}{\Lambda_T} = \frac{1}{\Lambda_A} + \frac{1}{\Lambda_S} \tag{4.4}$$

The main results are shown in Figures 4.16, 4.17, 4.18, 4.19, and 4.20. The first plot reports the nominal and measured refractive index; both were provided by the producer (and the precise numerical values are reported in Table 4.1). The second shows the mass density of the tiles as a function of the refractive index; clearly, there is a linear relation between them. The third shows the absorption length, which is not uniform for different tiles with the same refractive index. ~~This fact can be neglected~~ because the absorption

Tile ID	Producer	Production year	Refractive index		Side [mm]	Width [mm]
			Nominal	Measured		
TSA2-1a	Japanese	2021	1.020	1.0206	50	20.5
TSA1-2b	Japanese	2021	1.020	1.0206	50	20.8
TSA1-3b	Japanese	2021	1.020	1.0199	50	20.8
TSA2-4a	Japanese	2021	1.020	1.0204	50	20.8
TSA3-1a	Japanese	2021	1.030	1.0301	90	21.1
TSA3-2a	Japanese	2021	1.030	1.0303	90	21.0
TSA3-3a	Japanese	2021	1.030	1.0304	90	21.3
TSA3-3b	Japanese	2021	1.030	1.0304	90	21.1
AG22J001	Japanese	2022	1.020	1.0210	50	20.5
AG22J002	Japanese	2022	1.020	1.0201	50	20.6
AG22J003	Japanese	2022	1.020	1.0207	50	20.4
AG22J004	Japanese	2022	1.020	1.0218	50	19.5
AG22J005	Japanese	2022	1.015	1.0152	50	19.9
AG22J006	Japanese	2022	1.015	1.0158	50	21.7
AG22J007	Japanese	2022	1.015	1.0158	50	21.4
AG22J008	Japanese	2022	1.015	1.0158	50	21.4
AG22J009	Japanese	2022	1.024	1.0260	50	21.3
AG22J010	Japanese	2022	1.024	1.0261	50	21.2
AG22J011	Japanese	2022	1.024	1.0232	50	19.1
AG22J012	Japanese	2022	1.024	1.0232	50	19.4
AG22J013	Japanese	2022	1.020	1.0205	110	20.3
AG22J014	Japanese	2022	1.020	1.0208	110	20.3
AG22J015	Japanese	2022	1.020	1.0208	110	20.4
AG22J016	Japanese	2022	1.020	1.0207	110	19.7

Table 4.1: Recap of the aerogel tiles tested using the prototype. The values of the measured refractive index were provided by the producer. If the ID reported is **bold**, the correspondent tile was used to form a 4-cm-thick layer of aerogel in the prototype measurement.

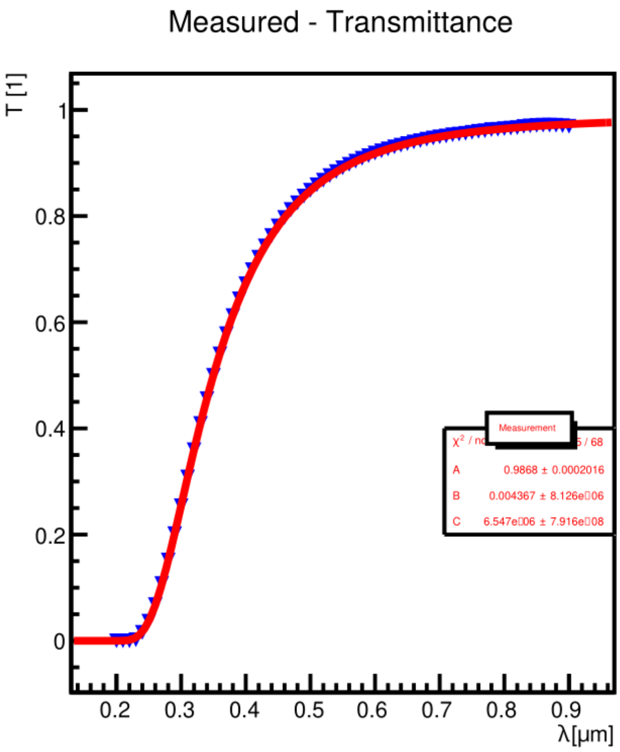

Figure 4.15: Measured transmittance (blue arrows) fitted using the extended Hunt formula (red).

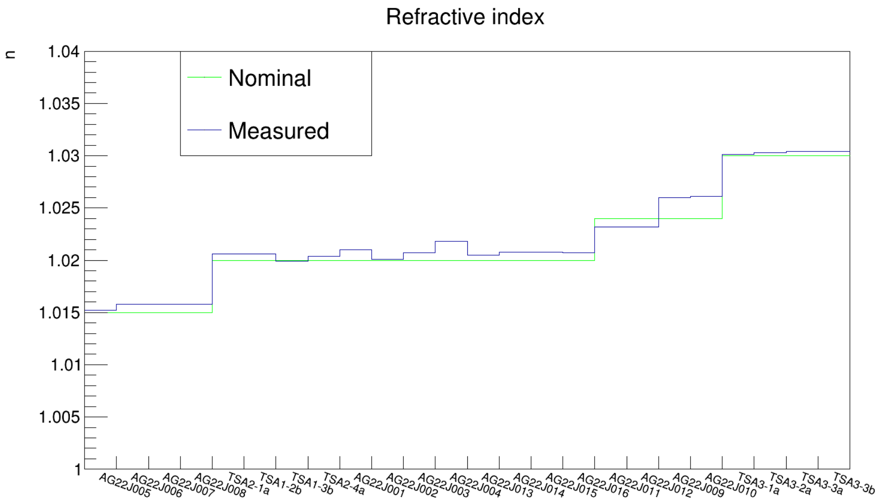

Figure 4.16: Refractive index of the aerogel tiles.

length is at least one order of magnitude longer than the scattering length, and then it has a second-order effect on the total transmission length. The last two plots describe the scattering and total transmission length, showing an almost linear correlation with the refractive index. This relation implies that in the studied range~~,~~ aerogel with a larger refractive index will have a larger yield of photons and better optical quality, ~~resulting~~ in a better single-particle resolution.

Not all the tiles characterized can be studied with the existing dRICH prototype. Indeed, the aperture of the Cherenkov cone produced by tiles with $n = 1.03$ is larger than the mirror acceptance, and the photons are not reflected onto the photo-detector. In addition, an aerogel with $n = 1.03$ has a poor momentum overlap with the gas radiator and is not suitable for the dRICH. The aerogel study is therefore limited to $n = 1.026$. The characterization results are used in the process of selecting the most uniform pairs of aerogel tiles to be tested with the prototype, in the anticipated ePIC configuration with a 4-cm-thick aerogel layer, corresponding to two stacked tiles. The final selection was based on the uniformity of the refractive index and maximization of the total transmission length. These conditions led to the definition of the pair of tiles for each nominal refractive index to be used during the test beams with the prototype. The selected tiles are highlighted in bold characters in Table 4.1.

Forward scattering measurement

Local inhomogeneities in the aerogel density or its micro-structure can affect the light propagation in the aerogel volume. This effect ~~is associated~~

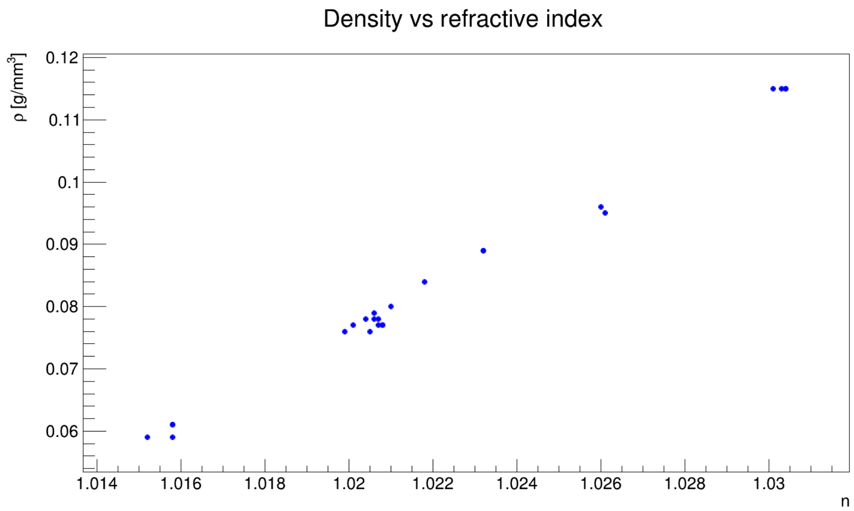

Figure 4.17: Density of the aerogel tiles versus the refractive index.

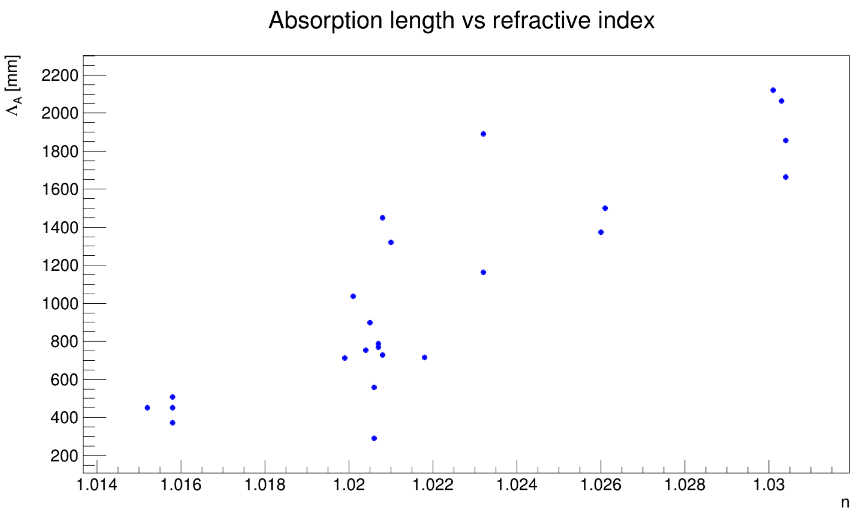

Figure 4.18: Absorption length of the aerogel tiles versus the refractive index.

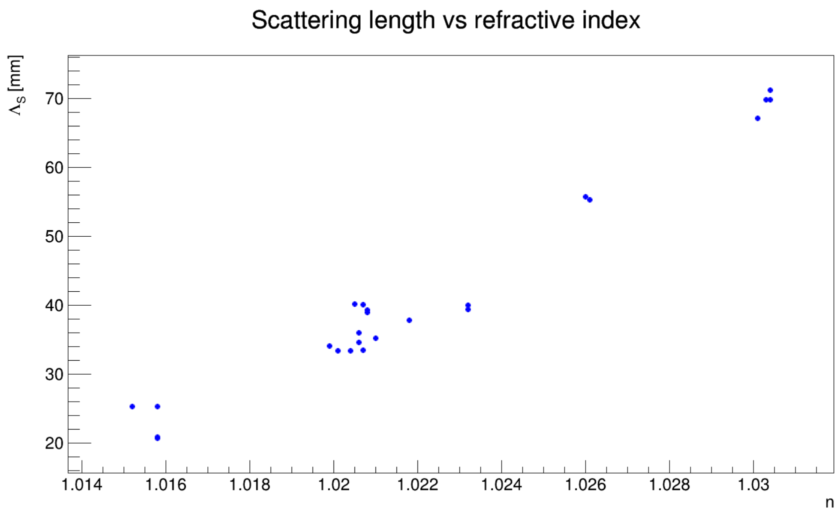

Figure 4.19: Scattering length of the aerogel tiles versus the refractive index.

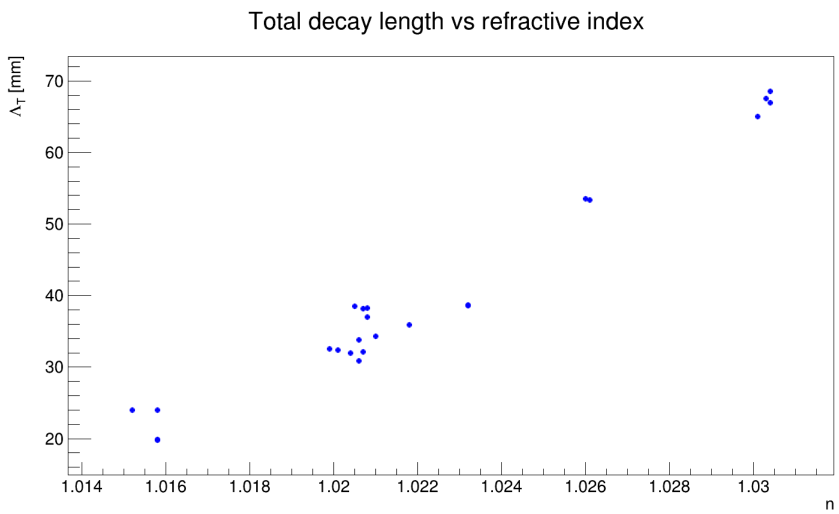

Figure 4.20: Total transmission length of the aerogel tiles versus the refractive index.

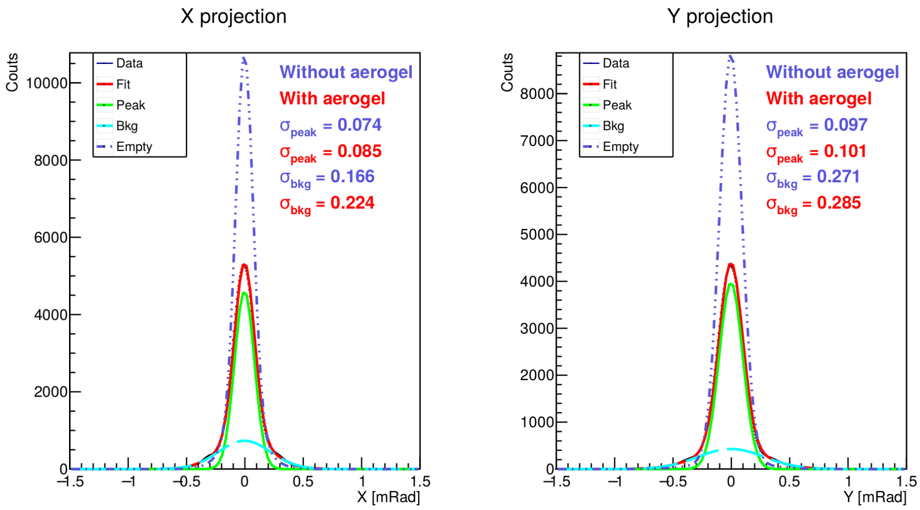

Figure 4.21: One-dimensional projection of the beam spot along x (left) and y (right) directions. In addition to the fit (red) and the two Gaussians (~~peak~~ green and ~~background~~ light blue), the curve of data without aerogel (~~blue~~) is reported.

with the enlargement of a laser beam spot passing through the aerogel sample, a phenomenon called forward scattering. It was studied by sending an attenuated laser beam through the sample directly to a CCD sensor, and acquired the beam spot for a grid of points along the aerogel surface. The comparison with the reference spot in the absence of the aerogel allowed the evaluation of the forward scattering. The analysis was conducted using the one-dimensional projection of the beam spot along the axes. These projections were fitted by a sum of two Gaussian functions associated with the laser spot and its halo. From plots in Figure 4.21, showing the mean of all the measurements compared with the reference curve, it is deducible that the forward scattering has a second-order effect on the laser spot.

Aerogel metrology

Another step of the characterization is the measurement of the size of the aerogel tile, ~~particularly the thickness~~. The measurement was performed by the mechanical workshop of the INFN Ferrara and analyzed by the author. The result is shown in Figure 4.22. The distribution of the two faces of the same tile shows one is concave and the other convex. This fact can explain ~~why there is~~ a systematic difference in the Cherenkov angle values and resolutions obtained by swapping the ~~side~~ of the aerogel tile. The plots showing the systematic differences are reported in Figure 4.23 and 4.24.

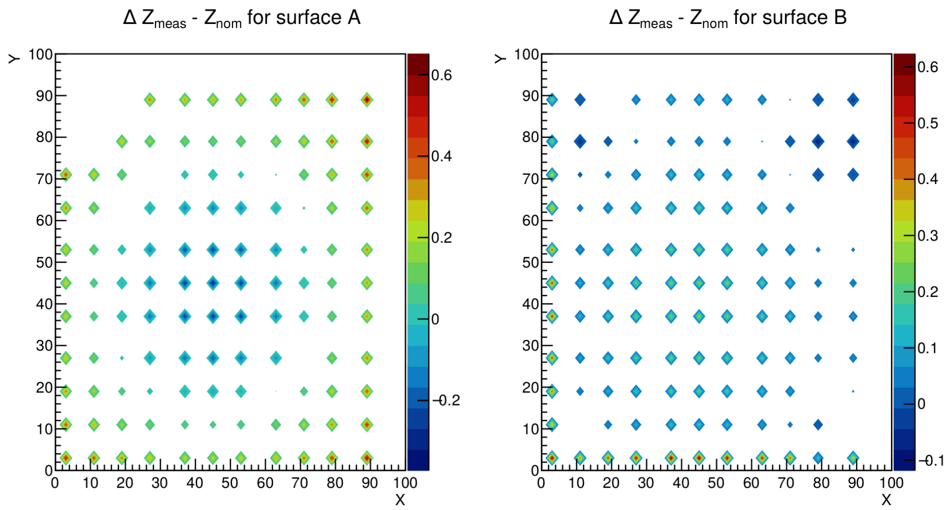

Figure 4.22: Difference between the measured thickness of aerogel and the nominal expectation. The left and right plots show the two faces of the same tile.

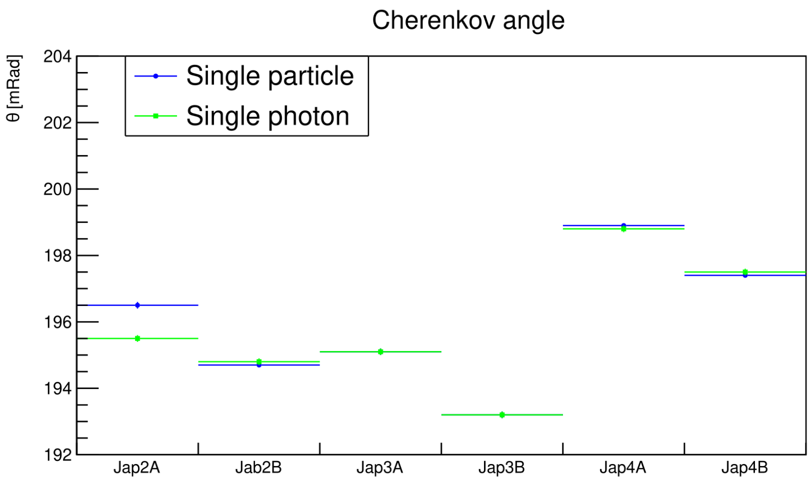

Figure 4.23: Cherenkov angle measured for different aerogel tiles with nominally the same refractive index. The letters A and B identify the entry face of the tile. ~~Changing~~ from side A to B ~~means~~ a Cherenkov angle smaller by $\sim 2\,\mathrm{mRad}$.

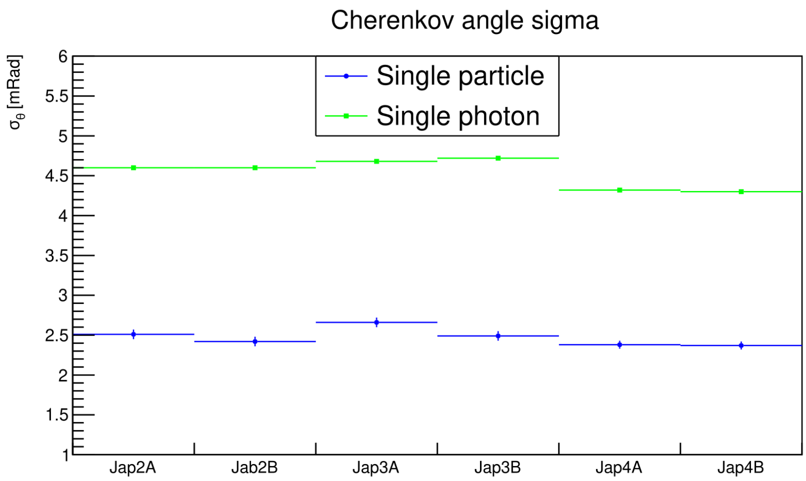

Figure 4.24: Resolution on the Cherenkov angle measured for different aerogel tiles with nominally the same refractive index. The letters A and B identify t~~he~~ entry face of the tile. ~~Change~~ from side A to B ~~means~~ obtaining the same or smaller resolution.

4.3.3 Simulation

A simulation was developed using GEant4 Monte-Carlo (GEMC) [33][47], a framework dedicated to the simulation of low and medium-energy particle physics, to evaluate the performance of the dRICH prototype. A relatively simple model of the prototype was implemented using CAD drawings of the main elements and textual implementation of their physical properties (material, density) and optical properties like reflectivity (mirrors), Rayleigh scattering, refractive index, and total transmission length (aerogel and gas). The photo-detectors were simulated as a solid plane absorbing all the photons in a thin thickness; the effects of quantum efficiency and pixelation were applied during the analysis. The elements of the prototype model are shown in Figure 4.25. In addition to the main components of the dRICH, the simulation model includes two objects representing the GEM detectors composing the tracking system employed at the test beams. This model was used during the design phase to establish the value of some important parameters, like the curvature radius of the mirrors, and for the preliminary evaluation of the expected Chernkov angle resolution achievable with the prototype.

The simulation ~~does~~ not perfectly reproduce the prototype; for example, the simulated beam was punctiform and with no divergence, or the background was negligible with respect to the real case. The results provided by the prototype simulation ~~are~~ then too optimistic. ~~For this reason, the estimation provided by the dRICH simulation group~~ was used to evaluate the Cherenkov angle resolution achievable by the prototype. It is based on

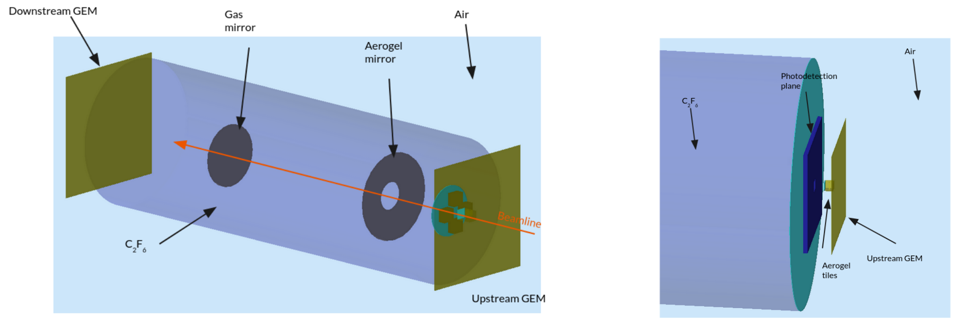

(a) Prototype simulation, full view

(b) Prototype simulation, detailed aerogel and photodetection area view

Figure 4.25: Prototype simulation draws.

the different contributions of the several error sources in a RICH detector:

- Pixel error, caused by the information loss due to the finite dimension of the photo-sensors pixel;
- Chromatic error, due to the dependence of the refractive index ~~by~~ the photon wavelength;
- Emission error, due to the uncertainty of the Cherenkov photon emission position inside the radiator;
- Tracking error, due to the global uncertainty associated with the track of the charged particle passing through the detector.

The values of these contributions can be found in Figure 4.26. It reports the estimated contributions to the Single PhotoElectron (SPE) resolution for the two radiators, divided into “Demo” (meaning prototype) and dRICH. The main difference between detector and prototype regards the contribution of the pixel error for aerogel. Indeed, in the dRICH the distance between aerogel and mirror is $\sim 1.2\,\mathrm{m}$, while for the prototype is $\sim 0.4\,\mathrm{m}$. It makes the relative uncertainty on the Cherenkov angle caused by the uncertainty on photon-position more relevant for the prototype.

The prototype’s total SPE resolution is expected to be 3.0 mRad for aerogel and 1.1 mRad for gas. For the dRICH, the expected values are 2.3 mRad and 1.0 mRad, respectively. The resolution on the single-particle mean Cherenkov angle can be obtained as

$$\sigma_{sing\_part} = \frac{\sigma_{SPE}}{\sqrt{N_{photons}}} \tag{4.5}$$

For the prototype, the σ_{sing_part} is expected to be 1.2 mRad for aerogel and 0.3 mRad for gas, using the previous values and the number of photons

1 p.e. error (mrad)		Aerogel		Gas	
		Demo	dRICH	Demo	dRICH
Pixel	(3mm pixel)	1.9	(0.6)	0.6	(0.5)
Chromatic	(300 nm filter)	1.8	(2.2)	0.6	(0.5)
Emission	(1 cm out of focus)	0.3	(0.3)	0.4	(0.6)
Tracking	(0.5 mrad)	0.4	(0.3)	0.4	(0.4)
Total		3.0	(2.3)	1.1	(1.0)

Figure 4.26: Table of the different contributions to the Cherenkov angle resolution. The values in the "demo" columns are theoretical estimations for the prototype, while the dRICH column is associated with the detector. The main difference regards the pixel effects for the aerogel because, in the prototype, the aerogel photons have to travel along a shorter path.

obtained from simulation. For the dRICH, these values became 0.7 mRad for aerogel and 0.3 mRad for gas.

For the dRICH, to achieve the requirements of a 3σ separation between pion and kaon in the high-momentum region, a resolution on the single-particle mean Cherenkov angle of 0.8 mRad for aerogel and 0.3 mRad for gas is needed. These requirements are taken from the dedicated talk at the last ePIC collaboration meeting, Reference [45]. The plots allowing to obtain these values are reported in Figure 4.27. A result of the prototype simulation, obtained using the optical properties of an aerogel with refractive index $n = 1.020$ and the single-particle resolution previously described, is shown in Figure 4.28. A recap of the achievable resolution according to the simulation can be found in Table 4.2.

Expected resolution	Aerogel		Gas	
	Prototype	dRICH	Prototype	dRICH
σ_{SPE} [mRad]	3.0	2.3	1.1	1.0
σ_{sing_part} [mRad]	1.2	0.3	0.7	0.3

Table 4.2: Recap of the SPE and single-particle resolutions achievable according the simulation.

4.3.4 Test beams

The prototype was tested in several test beams at the European Council for Nuclear Research (CERN) between 2021 and 2023 using the experimental halls available at Proton Synchrotron (PS) and Super Proton Synchrotron (SPS), accelerators providing beams of charged mixed hadrons, respectively, with momentum up to 11.5 GeV and up to 200 GeV. Aiming the dRICH to

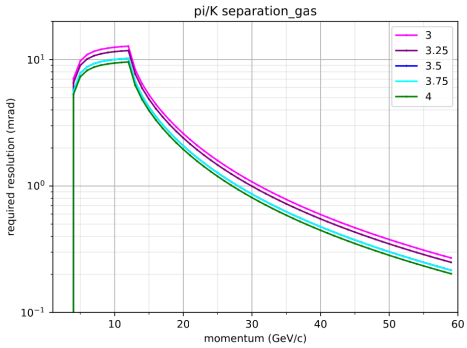

(a) Plot of single-particle mean Cherenkov angle resolution needed for the gas radiator.

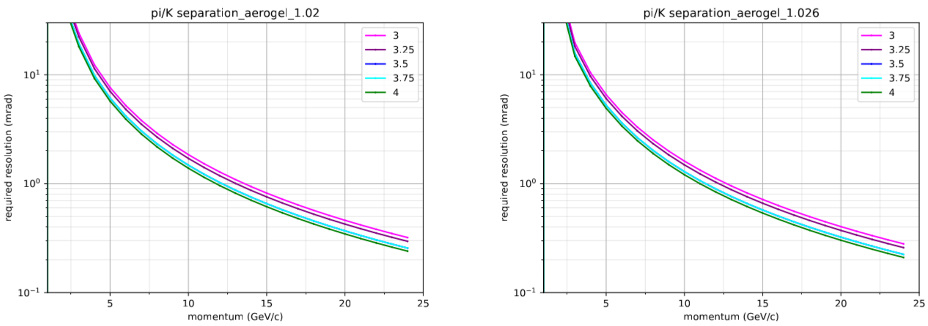

(b) Caption

Figure 4.27: Plots of the single-particle Cherenkov angle resolution needed for the dRICH to achieve the required resolution of at least 3σ. The plots are taken from reference [45].

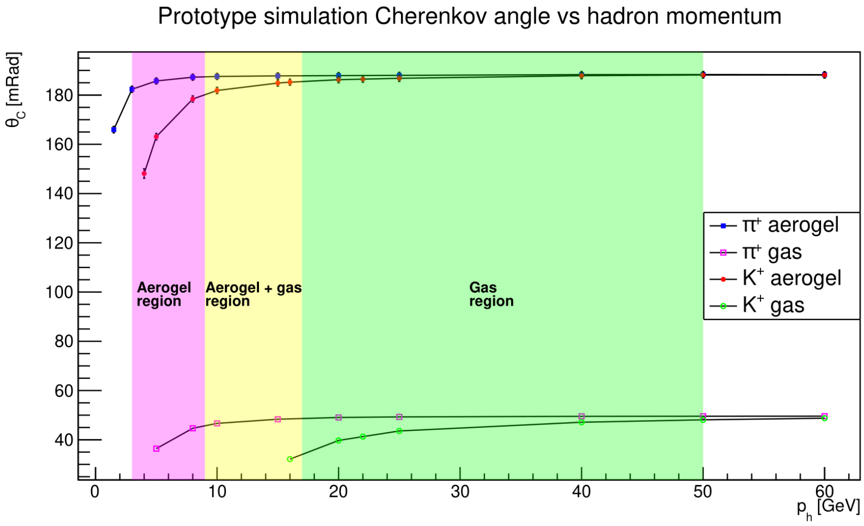

Figure 4.28: single-particle mean Cherenkov angle obtained from the simulation as a function of the hadron momentum, for positive pion and kaon. The error on the resolution was derived from ~~the $\sigma_{SPE} = 3.0$ mRad estimated by the dRICH simulation group~~. The magenta, yellow, and green areas highlight the region where the different radiators can be used to identify the particle.

distinguish particles with momentum up to 50 GeV and having the aerogel a refractive index larger than the C_2F_6 one, the test beams goals were:

- on both the experimental location, to perform studies on several aerogel tiles with different refractive index and stack compositions, applying wavelength filters and exploiting the Cherenkov threshold detectors of the beam to identify particles of different species with the dRICH;
- at PS, study the momentum interval common to the two radiators with a beam extended in space and divergence;
- At SPS, to measure the resolution with saturated rings and well-collimated particles.

During the first test beam in 2021, the SiPM detector box was used mainly to operate the photosensors, their cooling system, and the data acquisition chain. In the 2023 Fall test beam, the latest version of the SiPM detector box, represented in Figure 4.29a, allowed to obtain the first almost complete imaging of the double-ring of photons~~,~~ as shown in Figure 4.29b.

The MAPMT detector box was used during all the test beams to measure the prototype's performance and map the achievable resolution of aerogel and gas Cherenkov angles. The following sections will present the analysis developed and the results obtained.

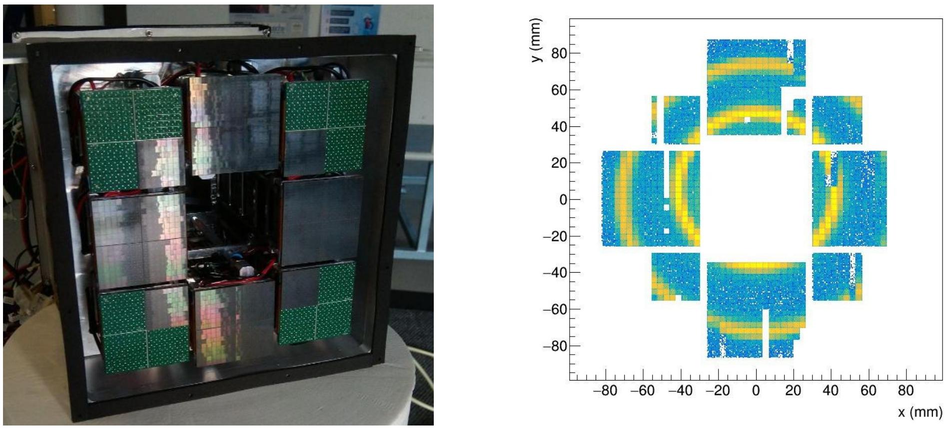

(a) Picture of the photo-detector side of the SiPM detector box.

(b) The two rings obtained in the last test beam using the SiPM detector box.

Figure 4.29: The latest version of the SiPM detector box includes 4 readout units with 256 sensors and 4 readout units with 64 sensors~~.~~ It allows the detection of almost the whole two rings, both from aerogel and gas.

Experimental setup

The test beam setup included a tracking system, a trigger apparatus, and external PID detectors from beam instrumentation; a picture of this is shown in Figure 4.30. The tracking is based on two Gas Electron Multiplier (GEM) detectors placed upstream and downstream of the dRICH. The GEM detects the position in which the beam crosses it, and the coincidence of the signals from the two detectors is used to find the track of the particle with a resolution better than 100 µm. The GEMs were a smaller version of those described in the Reference [26]. The GEMs had their power supplies providing high ($\sim 4\,\mathrm{kV}$) and low voltage, front-end boards, and data acquisition software; the author developed his expertise in operating the tracking system and became the expert-on-call since the 2022 test beams.

The trigger system was based on four finger scintillators measuring an area of $2 \times 1\,\mathrm{cm}^2$ each, two placed in front of the aerogel box and two just downstream of the prototype, and read with SiPMs. The components of each pair of scintillators work in coincidence to avoid random triggers. The logical AND and OR of the scintillator pairs were available for the trigger and could be selected from the control room without accessing the experimental hall. ~~The~~ GEMs~~' signals,~~ slower than the MAPMTs'~~ signals,~~ ~~were~~ used to veto new triggers until t~~hey~~ were ~~busy~~. This configuration allows the~~-~~pairing of the track with the corresponding dRICH event.

Figure 4.31 reports the plots relative to the tracking system from two runs acquired at the two accelerators, showing clear differences. The beam profile and the divergence of the SPS beam are smaller than the PS beam.

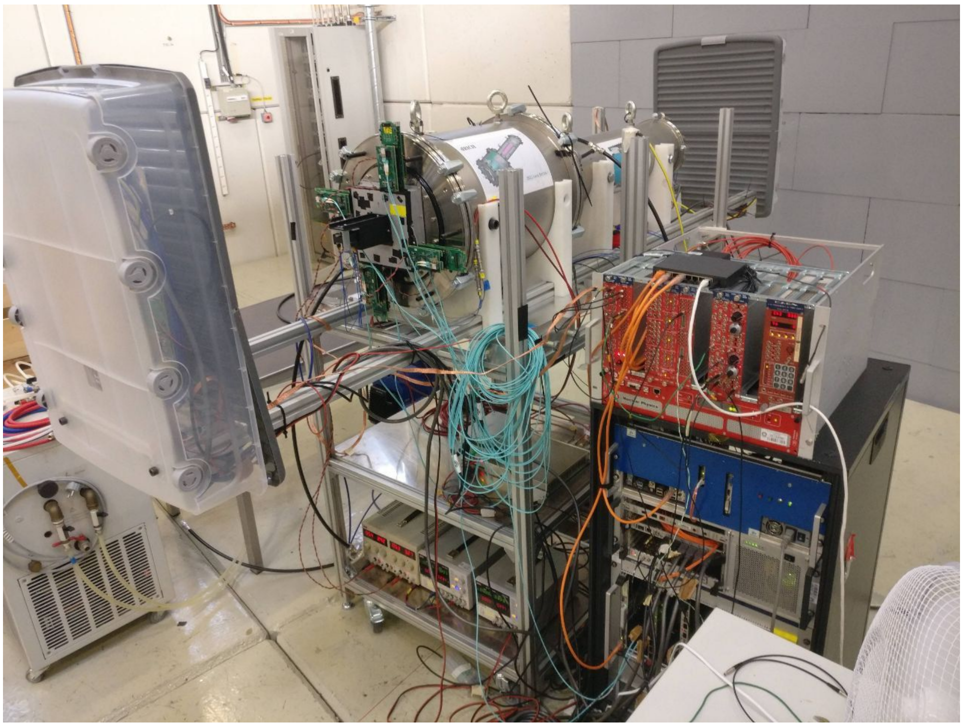

Figure 4.30: Experimental setup of the 2023 test beam at PS. The beam income from the left side. From the left to the right of the picture, it is possible to find the upstream GEM, inserted in the safety box to mitigate the high-voltage risk; the mechanical structure sustaining the detector, which is adjustable in height and inclination; the aerogel container, that is the small 3D-printed black box; the MAPMT box, in the "corner" configuration as deductible from the position of the electronic boards; the cylinders constituting the dRICH, which are filled of C_2F_6; and the second GEM inside the safety box. Also visible are the light blue optical fibers, for the communication of the MAROC readout with the storage; the power supplies, both for the readout electronic and for the tracking; the black pipe of the gas distribution system; the electronics boards handling and merging the tracking, trigger, and beam Cherenkov signals. The beam Cherenkov detectors are part of the beamline upstream of the prototype and are not visible.

At PS, the coincidence with the trigger scintillators is also used to limit the beam profile, which could also be larger than the one shown in Figure 4.31b; instead, at SPS, the beam spot is smaller than the area covered by the trigger system.

The test beam setup included an external PID apparatus consisting of two (at PS) or three (at SPS) gaseous threshold Cherenkov detectors. They can host various gases and adjust the inner pressure, modifying the refractive index. This procedure permits setting a threshold for the mass of the particles producing the Cherenkov photons for a given beam momentum. Particles lighter than the threshold will produce light inside the detector, while heavier particles will not. Combining the information from various detectors with different settings makes it possible to tag different species of particles. For example, a detector activation scheme for the PS is reported in Table 4.3. The signals provided by the trigger signal and the beam Cherenkov were

Particle	Threshold $\leq m_K$	Threshold $\leq m_p$
π	✓	✓
K	✗	✓
p	✗	✗

Table 4.3: Example of beam Cherenkov threshold settings. The combined information permits the identification of the hadron passing the detector.

read using a special adapter board coupling them to the MAROC, the same readout of the MAPMT. This allowed us to handle them easily with the same data acquisition software as the photo-detector.

The MAPMT box design supports two different configurations, called *cross*, with the photo-detectors placed close to the side of the central aerogel tile, and *corner*, with the photo-detectors placed at the corner of the aerogel tile. The two configurations were used because the MAPMTs in the cross configuration cover almost the whole gas ring but only $\sim 40\%$ of the aerogel ring; moreover, the aerogel ring is close to the external edge of the photodetection area for the nominal refractive index of the original design ($n = 1.020$). The corner configuration permits covering the rest of the aerogel ring, and to study aerogel with a larger refractive index (1.023, 1.026) characterized by better transparency properties but does not provide acceptance for the gas ring. The plots of the rings acquired in cross and corner configurations are visible in Figure 4.32.

Data analysis

The author wrote the data analysis software in `C++`, using the analysis framework ROOT by CERN. The software is based on modular logic, so new information can be added at each step, allowing access to them along the entire analysis chain. It was designed this way because the software has been

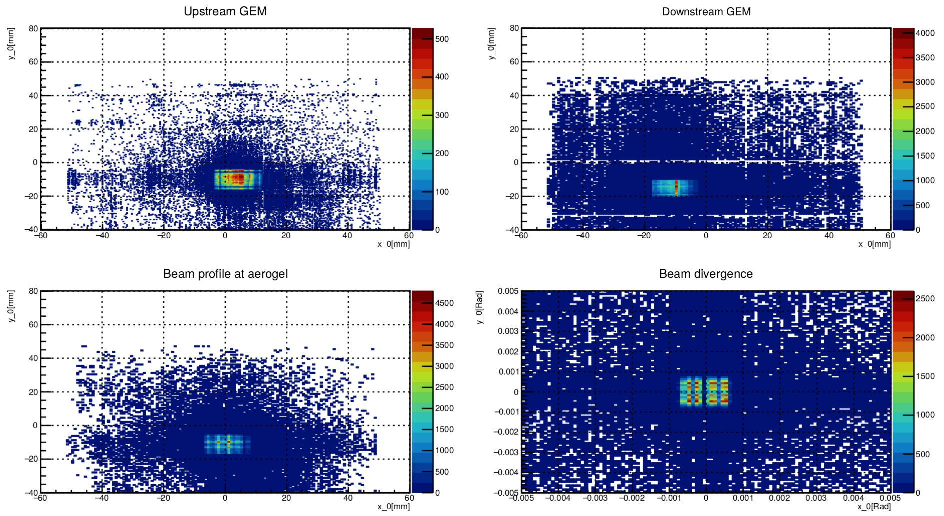

(a) The tracking plots for one run at SPS. The top plots show the beam profile in the two gems; the bottom plots show the extrapolated beam profile at the aerogel position and the divergence of the beam.

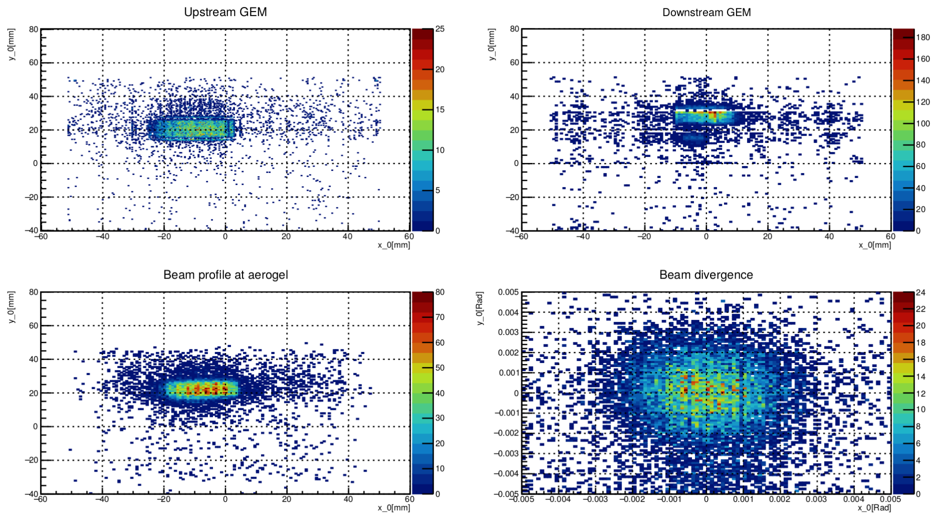

(b) The tracking plots for one run at PS. The top plots show the beam profile in the two gems; the bottom plots show the extrapolated beam profile at the aerogel position and the divergence of the beam.

Figure 4.31: Comparing the top and bottom plots, it is visible that the beam spot at SPS is smaller ~~rather~~ than at PS, and also it is smaller than the trigger $20 \times 10\,\text{mm}^2$, although ~~h~~ ~~the signal is noisier~~. Moreover, the divergence of the SPS beam is less than half ~~in radiu~~s of the PS~~,~~ The GEM allows cleaning the data sample from spurious events with secondary interactions (high-angle traces).

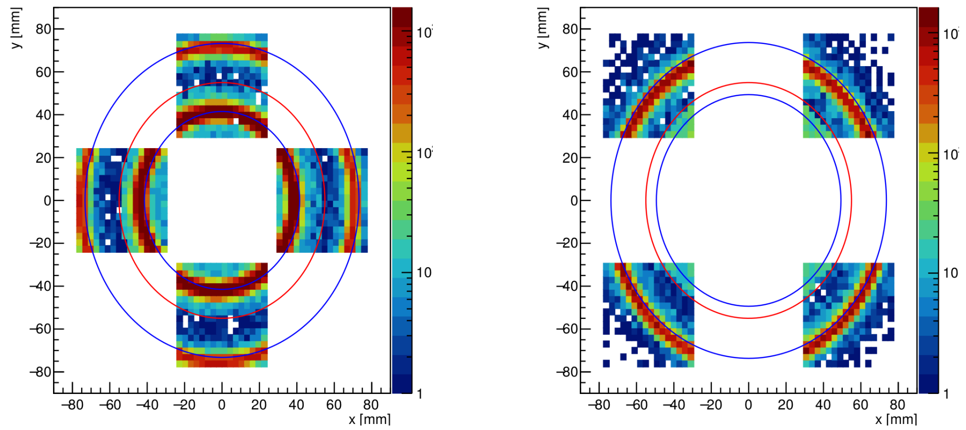

(a) Cumulated rings in the cross configuration.

(b) Cumulated rings in the corner configuration.

Figure 4.32: The two configurations of the MAPMT detector box. On the left, the two rings produced in gas and aerogel are visible. On the right, the ring produced by the aerogel is in the center of the photo-detectors and the gas ring is outside acceptance. The blue circles are the ring reconstructed during the analysis for gas (inner) and aerogel photons (outer), and the red one is the geometrical selection that is part of the photon assignment to the corresponding radiator.

developed over the years, starting from the first test beams in 2021, making it easier to introduce modifications. The software performs the following operations:

- Reconstruction of the photon hits by coupling the signal falling and rising edges and applying time calibration;
- Selection of real photons based on the hit duration (time-over-threshold);
- Distinction of the photons produced in aerogel and gas based on their time-of-flight and a geometrical cut on the radius;
- Selection of ring photons using the time-coincidence technique;
- Computation and application of a primary correction of photon position for small misalignments of the mirrors, computing the mean ring center for each run based on the distribution of the hit position;
- If the tracking information is available, computation and application of a secondary correction of the position of each photon based on the misalignment of the beam particle from the nominal ~~center~~ of the beamline;
- Averaging over the photon information associated with the particle, computation of the mean Cherenkov angle and time;

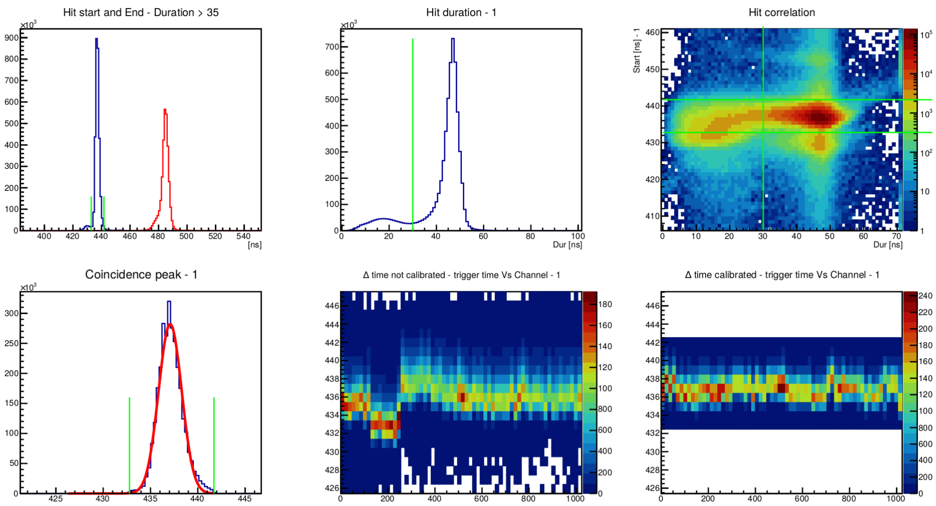

Figure 4.33: Plots summarizing the analysis operation to identify and assign the photon hits to the gas ring.

- Computation of the single-photon resolution, single-particle resolution, and its relation with the number of photons detected;
- When the beam Cherenkov detectors are available, computation of the same results for tagged particle species.

The assignment of photons to the ring is carried out in two steps. A preliminary distinction is based on a geometrical selection by defining "gas photons" as those with a radius lower than 55 mm and "aerogel photons" as the others. This permits the identification of two time-coincidence peaks, with a detectable difference of ~ 7 ns; the standard deviation of both peaks ~~is~~ ~ 1.2 ns. ~~Then, belonging to the~~ time-coincidence ~~peak became~~ the main criterion for assigning the photons to the right ring. Figure 4.33 summarizes the operation performed by the software on the hit. It includes the distribution of the start and end time of the hit, the hit over-threshold duration with the green line representing the selection to exclude the short signals generated by cross-talk, the coincidence peak of photons belonging to the ring, and the effect of the time calibration.

The main condition to be satisfied to consider a ring as good is that it includes at least 3 photons. A second selection is based on the divergence of the beam track, which is estimated as the trajectory-difference with respect to the line connecting the center of the beam spots in the two GEMs. Incident particles with a polar angle larger than 2 mRad are removed from the sample.

The primary correction on the photon position was developed to compensate for small misalignments of the mirrors with respect to the detector axis. The correction starts from the computation of the mean optical center of the event, obtained by averaging the x and y coordinates of all the photons hitting the MAPMTs. This operation is made separately for gas and aerogel rings because the mirrors are not coupled, so they can affect the photon direction differently. The mean center is taken as the origin of the ring coordinate system, and the position of the photons is shifted accordingly.

The event-by-event correction based on the particle track divergence with respect to the beam ~~center~~ was developed after the first test beam when a correlation between the particle incident angle and the ring position was noted. This permits the extrapolation of the correct center of the ring associated with the particle, by composing the global correction plus the projection of the single particle emittance. The effect of the two corrections can be neglected, reducing the resolution by up to one-third.

The data acquired using a mixed-hadron beam of 120 GeV, momentum at which both the aerogel and gas rings are saturated for any particle species, are considered to explain the output of the analysis. In Figure 4.34, the first plot shows the distribution of the single-particle mean Cherenkov angle, the mean time of the photons associated with the particle, and the distribution of the number of photons for the particle. The first of these distributions is fitted with a Gaussian, whose mean value is taken to be the Cherenkov angle associated with the particle momentum, and the standard deviation is taken to be its resolution. The first and the second ~~raw~~s show the ~~plot~~ for gas (on top) and aerogel (bottom). From these plots is possible to compare the prototype results and the values expected from simulation, ~~that were~~ adapted to be analyzed by the same software.

Additional results produced by the analysis are shown in Figure 4.35. The left ones are the distribution of the reconstructed Cherenkov angle of each photon associated with the ring for gas (on top) and aerogel (bottom), fitted again using a Gaussian function where the mean corresponds to the Cherenkov angle and the standard deviation with the single-photon resolution. The right plots show the single-particle resolution as a function of the number of photons associated with the ring. This graph is fitted with the function

$$\sigma_{sing\_part}(n_\gamma) = \sqrt{\frac{p_0^2}{n_\gamma} + p_1^2} \tag{4.6}$$

where parameter p_0 represents the single photon resolution, the best resolution achievable with only one photon, and p_1 is the asymptotic single-particle resolution, the minimum value achievable in an ideal situation of infinite photons. These plots allow the comparison of the SPE resolution obtained from two different methods and the analysis of the possible residual contribution to the resolution: a non-zero p_1 value signals systematics effects like misalignment or non-uniform detector response. The specific results for aerogel and gas and their comparison with simulation are commented in the next Section.

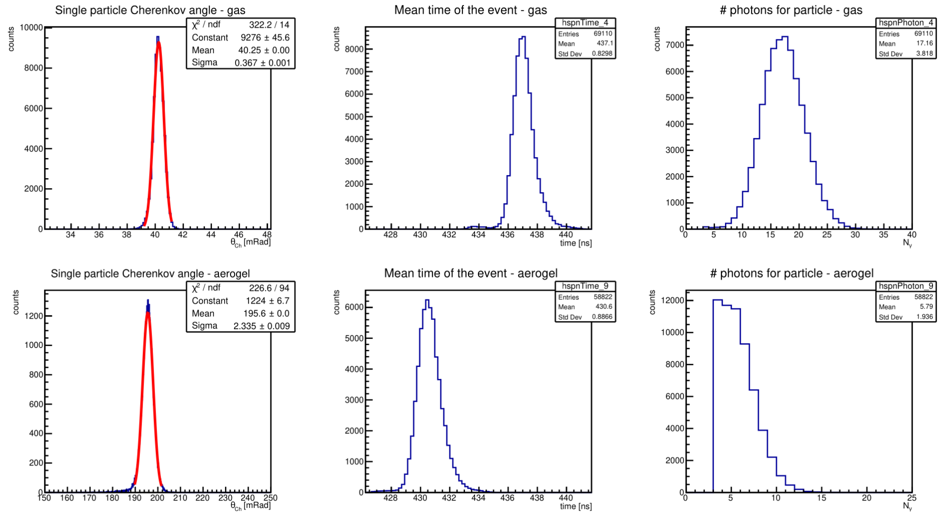

Figure 4.34: Example of the results of the prototype analysis, for the case of a 120 GeV beam of mixed hadrons. From left to right: the distribution of single-particle mean Cherenkov angle, the distribution of the mean time of photons, and the distribution of the number of photons for particle. In the top row are the plots for gas, and in the bottom row the plots for aerogel. In the rightmost column the partial coverage of the aerogel ring is evident.

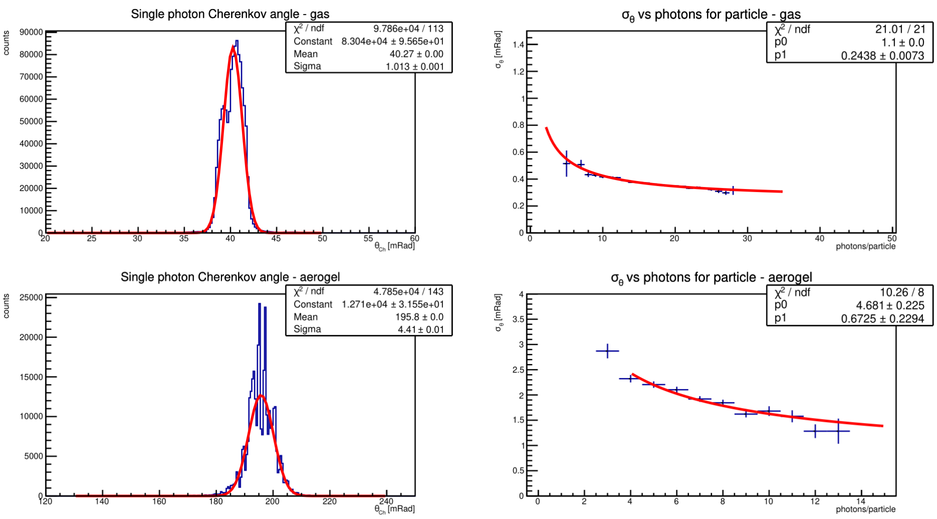

Figure 4.35: Example of the typical results of the prototype analysis, for the case of a 120 GeV beam of mixed hadrons. From left to right: the distribution of SPE Cherenkov angle resolution and the single-particle resolution vs the number of detected photons. In the top row are the plots for gas, and in the bottom row are the plots for aerogel.

4.4 Results of the prototype studies

In this section, the measured performances of the prototype are reported and compared with the expected values provided by the simulation. The simulation described in section 4.3.3 is the newest version of the prototype simulation. It has been described because of its importance in the design phase and because the author developed it. Despite being the last version, it is still optimistic and reproduces the prototype only partially. This implies that ~~the~~ simulated resolution is better than the one achievable with the prototype. For this reason, the plots resulting from the analysis of the simulation are shown in this Section, but the main comparison to evaluate the resolution achieved by the prototype is made with the values taken from Table 4.2.

4.4.1 Results for gas ring

The data selected to study the gas resolution were acquired at SPS using the mixed-hadrons 120 GeV beam. The plots of the single-particle mean Cherenkov angle and of the number of photons detected for particle are reported in Figure 4.36; the top row is for data, and the bottom row is for simulation. The Cherenkov angle shows a small difference ($\sim$ 4 mRad) between the simulation and the data, which could be explained by small differences between the mirror curvature radius of the simulation and the real mirror, or by small differences between the gas description in simulation and its real values of pressure and refractive index. The best single-particle resolution achieved with the prototype is 0.35 mRad, approximately two times the correspondent value obtained from the prototype simulation~~,~~ 0.17 mRad. Comparing it instead with the most reliable value of 0.3 mRad reported in Table 4.2, they are closer. ~~These~~ values could improve further by applying a most refined reconstruction algorithm, ~~maybe~~ the ray-tracing algorithm developed by the dRICH simulation group, and testing the prototype with the SiPM detector box, because the silicon-based sensors are less sensitive to the chromatic contribution to the error rather than the MAPMT~~,~~ The mean number of photons detected from the prototype is smaller than the expectation from the simulation, 17.1 compared to 20.3.

The plots in Figure 4.37 show the same differences on the reconstructe~~d~~ Cherenkov angle, which is 4 mRad smaller for simulation, and on the SPE resolution, which is 2 times larger for the prototype rather than the simulation. As in the single-particle case, the SPE resolution measured is ~~according to~~ the estimation described in Section 4.3.3 because it is 1.1 mRad ~~for data~~ for both the ~~possible~~ methods (Gaussian ~~fit σ and parameter p_0 on the right plot fit~~). The parameter p_1 assumes non-zero values both in data (0.24 mRad) and simulation (0.03 mRad). It signals systematic effects like non-uniform detector response or a misalignment not recovered by the~~-~~correction~~,~~. ~~The difference between the two values of~~ p_1 could mean that both a misalignment

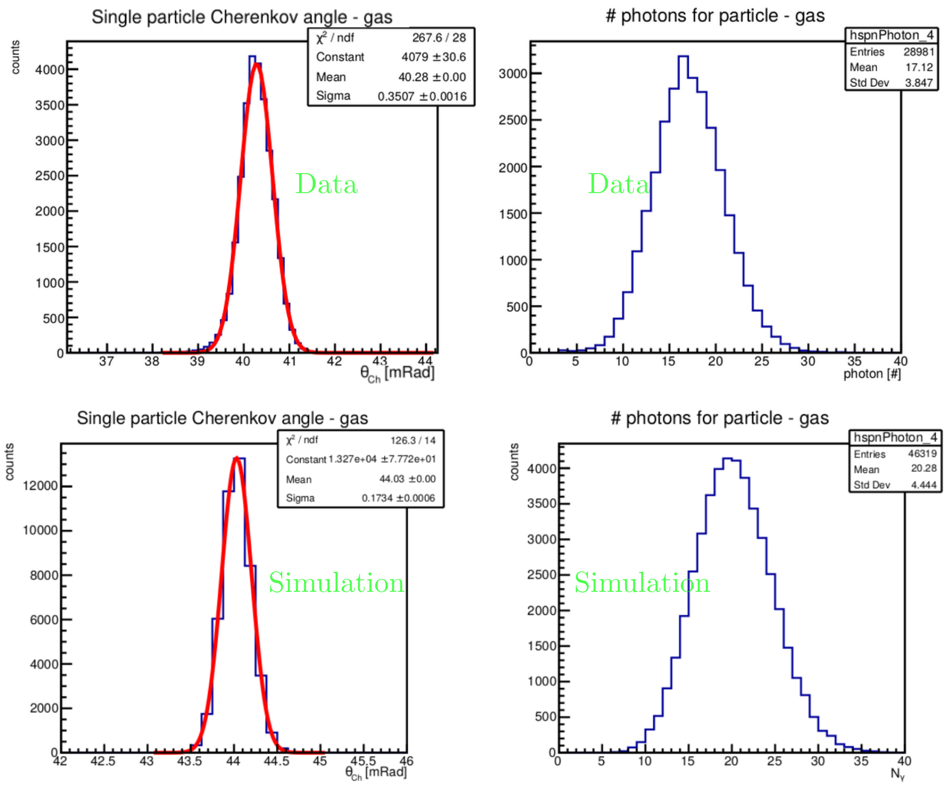

Figure 4.36: Single-particle results for gas ring. From left to right: the single-particle mean Cherenkov angle, and the number of photons detected. On the top row are plots obtained from data, and on the bottom are plots from the simulation.

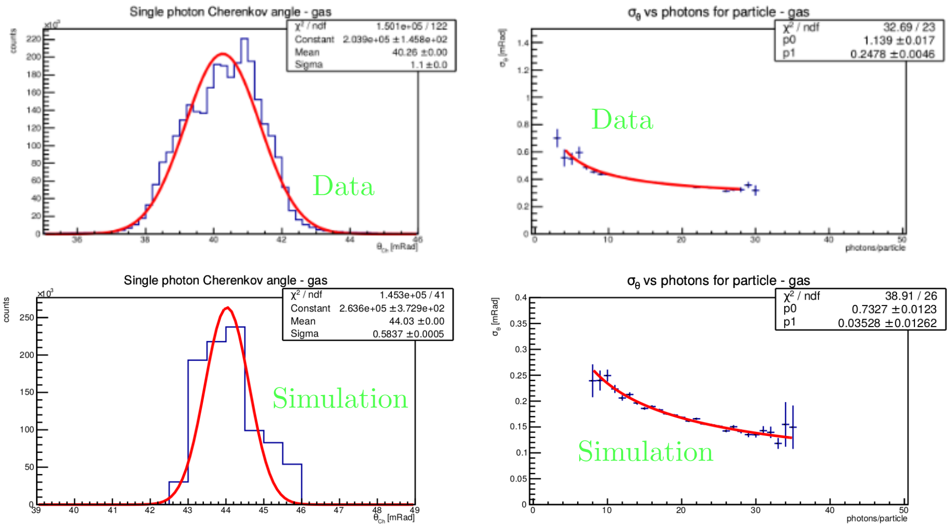

Figure 4.37: Single-photon results for gas ring. From left to right: the single-photon mean Cherenkov angle, and the single-particle resolution as a function of the number of photons detected. On the top row are plots obtained from data, and on the bottom are plots from the simulation.

and a systematic non-uniformity concur in the prototype.

4.4.2 Results for aerogel ring

The data selected to study the aerogel ring were acquired using a negative mixed-hadrons beam at 10 GeV. For this momentum value, the dominant component of the beam is constituted by pions, while kaons and antiprotons are in the order of a few percent. Although the aerogel ring is not fully saturated, this negative beam provided the best combination between a clean pion sample and luminosity to acquire enough statistics during the August 2023 test beam. Figure 4.38 shows the single-particle mean Cherenkov angle and the number of photons ~~for~~ particle plots, Figure 4.39 shows the single-photon Cherenkov angle distribution and the plot of single-particle resolution as a function of the number of ~~photons for particle detected~~. In both Figures, the first row reports the results obtained using the aerogel with refractive index $n = 1.026$, the second uses the design aerogel with refractive index $n = 1.020$, and the third row shows the simulation plots. This has been made because the aerogel with a larger refractive index showed better performance in the resolution and number of photons, as expected from the results of the characterization performed in the laboratory.

The single-particle and single-photon resolution achieved using the $n = 1.026$ aerogel are 2.0 mRad and 3.4 mRad, while for the $n = 1.020$ aerogel are 2.8 mRad and 4.7 mRad. The resolution obtained from the simulation plot ~~is~~ similar to the estimation reported in Table 4.2 for the single-particle resolution, 1.4 mRad versus 1.2 mRad, but is too optimistic for the single-photon resolution extracted using the left plot, that is 2.3 mRad versus the estimation of 3.0 mRad. The single-photon resolution extracted by fitting the rightmost column plots is less reliable in this case because of the low number of points that make the curve more approximable with a linear dependence. This is confirmed by the relative errors on parameter p_0 (Equation 4.6), which are one order of magnitude larger ~~rather~~ than the case of the gas ring. A deeper and more completed analysis will be performed using the SiPM detector box in the last version, which covers almost the full aerogel ring, allowing the detection of more photons. The values of the p_1 parameters ~~allow us to hypothesize~~ that the constant term present for the gas is zero for the aerogel. This is possible because the two rings are ~~completely~~ decoupled in the prototype, and then it is possible there is a systematic effect on the gas section that is not present in the aerogel section. Regarding the number of photons, there is an agreement between the simulation and the data acquired for $n = 1.020$ aerogel with a mean of 5.2 photons while using the $n = 1.026$ aerogel 8.0 photons for particle are detected, as expected from the characterization results.

The numerical results are summarized in Table 4.4. It shows that the prototype performance almost satisfies the expectations for both gas and aerogel. The gas SPE resolution of 1.1 mRad has been obtained since the 2022 test beam. Alternative developments will be studied with the updated prototype designed to test alternate gas mixtures and non-greenhouse pressurized gases. For the aerogel ring, the best SPE resolution obtained till the 2022 test beams was about 4.5 mRad, 1.5 times worse than the expected value of 3.0 mRad. The study performed in the 2023 test beam, described in the following, achieved a SPE resolution of 3.4 mRad, which is close to the design goal.

Future developments of the reconstruction software, for example, by implementing a ray-tracing algorithm to reconstruct the single-photon path, will allow further refinements in the resolution study.

4.4.3 Aerogel study with the prototype

The goal of the August 2023 test beam was to a detailed study of the aerogel resolution, having prior performed the laboratory characterization described in section 4.3.2. Using the aerogel samples from Aerogel Factory Co. highlighted in Table 4.1 and the two *corner* and *cross* configurations of MAPMTs, data were acquired for refractive index between $n_{min}1.016$ and $n_{max} = 1.026$. Figure 4.40 shows the measured single-photon and single-particle resolutions. From both plots, it is possible to see that by increasing the refractive index, the resolution improves; in particular, for $n = 1.026$, the SPE

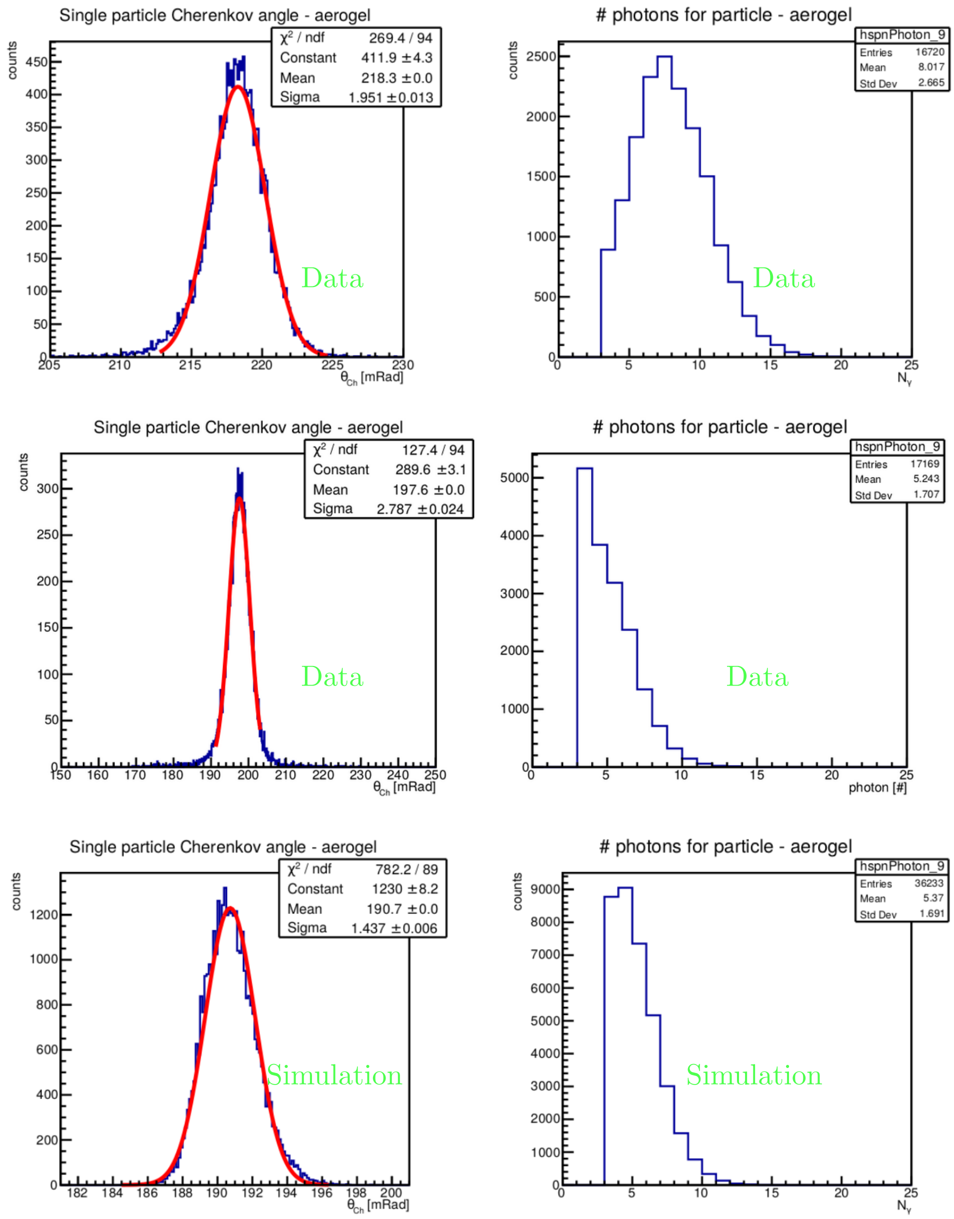

Figure 4.38: Single-particle results for aerogel ring ring. From left to right: the single-particle mean Cherenkov angle, and the number of photons detected. On the top row are plots showing the best resolution obtained using tiles with refractive index $n = 1.026$; in the middle row are plots showing the results obtained using tiles with refractive index $n = 1.020$; the bottom plots are derived from the simulation.

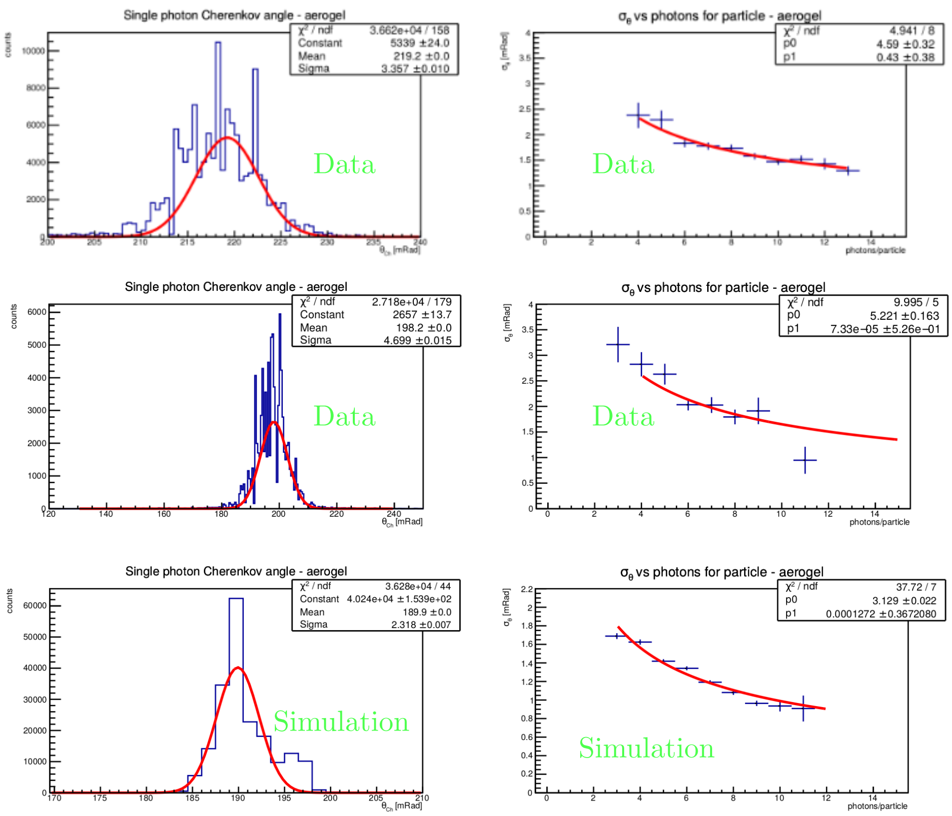

Figure 4.39: Single-photon results for aerogel ring. From left to right: the single-photon Cherenkov angle, and the single-particle resolution as a function of the number of photons detected. On the top row are plots showing the best resolution obtained using tiles with refractive index $n = 1.026$; in the middle row are plots showing the results obtained using tiles with refractive index $n = 1.020$; the bottom plots are derived from the simulation.

Summary table of the prototype performance					
Source	SPE σ [mRad]	Single-particle σ [mRad]	Photons/particle	p_0 [mRad]	p_1 [mRad]
Gas					
Data	1.10 ± 0.01	0.351 ± 0.002	17 ± 4	1.14 ± 0.02	0.248 ± 0.005
Simulation	0.584 ± 0.001 / 1.1	0.173 ± 0.001	20 ± 4	0.733 ± 0.012	0.035 ± 0.012
Aerogel					
Simulation	2.32 ± 0.01 / 3.0	1.44 ± 0.01	5.4 ± 1.7	3.13 ± 0.02	0.0 ± 0.4
Data $n = 1.020$	4.70 ± 0.02	2.79 ± 0.02	5.2 ± 1.7	5.22 ± 0.16	0.0 ± 0.5
Data $n = 1.026$	3.36 ± 0.01	1.95 ± 0.01	8 ± 3	4.6 ± 0.3	0.4 ± 0.4

Table 4.4: Table summarizing the performance of the prototype. The error reported is the statistical error provided by ROOT for quantities extracted by a fit, and the standard deviation for the number of photons. A cut-off on the third digit is applied in case of small errors. The Single PhotoElectron (SPE) column includes two values: the former is obtained from the prototype simulation, and the latter is the estimation provided by the dRICH simulation group for the prototype.

resolution measured is 3.4 mRad, which is the best result achieved. Figure 4.41a shows the number of photons for particle detected by the prototype as a function of the refractive index; as expected from the increasing of density and transmission Λ_T, aerogel with larger refractive index yields more photons. Figure 4.41b completes the results of this study, showing the measured Cherenkov angle that grows naturally with the increase of the refractive index. This study showed that aerogel with a larger refractive index provides more defined rings. Motivated by these results, the ePIC simulation group initiated a study to evaluate the impact of increasing the aerogel refractive index.

4.4.4 Studies using the beam PID system

The beam PID system described in section 4.3.4 permits ~~the tagging of~~ the hadron species passing through the detector with good efficiency and therefore the direct study of the prototype PID capability. For the gas component, this study used a beam of positive mixed hadrons with a momentum of 20 GeV and 50 GeV, covering the momentum range over which the identification is based on that radiator. The largest beam component is constituted by pions, followed by protons; the kaons are just a few percent, and they are detected by the prototype. The single-particle Cherenkov angle distribution for tagged hadron species is shown in Figure 4.42 and Figure 4.43. At 20 GeV, the kaon peak is clearly separated from the pion one. At 50 GeV, the proton peak appears, while the kaon starts to overlap with the pion peak. In both cases, a small inefficiency of the beam PID system is visible but does not affect the result.

The aerogel component was studied using beams of mixed positive hadrons with $6, 8$, and 10 GeV momentum. The plots are reported in Figure 4.44, Figure 4.45, and Figure 4.46. In this case, the beam Cherenkov had more inefficiencies, but the peaks of the three species are still visible. These data were acquired with the $n = 1.026$ aerogel, and the MAPMTs in the *corner* configuration, for which any information from the gas is lost. Comparing the three plots, the modification of the beam composition with the energy is also visible: protons became the major components at 10 GeV while the kaons represent always a small fraction (few percent).

These results confirm the capability of the prototype to detect and identify different particle species.

4.5 Conclusions

The Electron-Ion Collider is designed to expand the frontiers of the known Quantum Chromodynamics. Colliding high momentum and highly polarized beams with a high luminosity will produce data allowing unprecedented studies of the nuclear structure and parton dynamics. This can be done

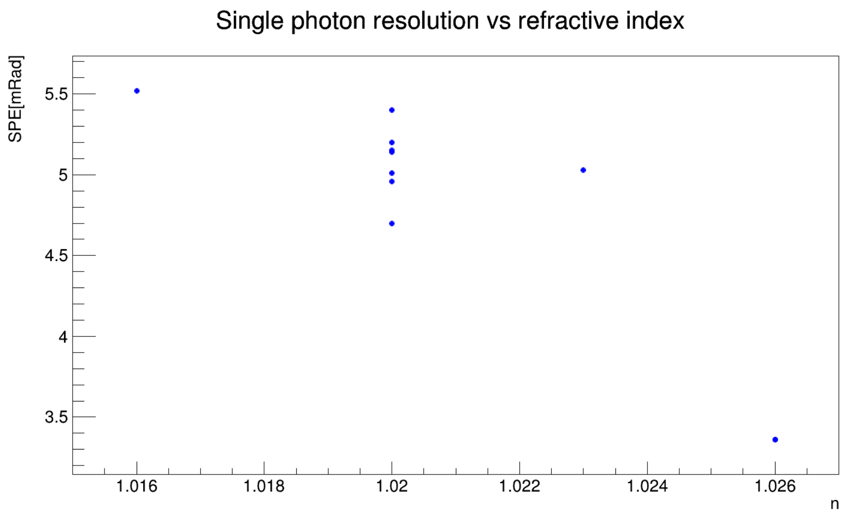

(a) Single photon resolution measured by the prototype using aerogel with different refractive index. The cluster of measurement at $n = 1.020$ is due to the fact that several tiles with this refractive index were tested, and the result from the 2022 test beam was also included.

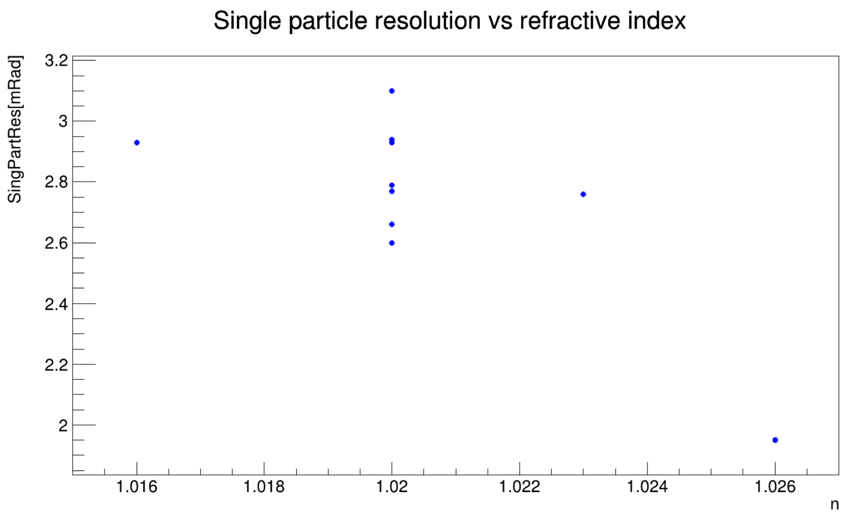

(b) Single-particle resolution measured by the prototype using aerogel with different refractive index. The cluster of measurement at $n = 1.020$ is due to the fact that several tiles with this refractive index were tested, and the result from the 2022 test beam was also included.

Figure 4.40: Results of 2023 aerogel study

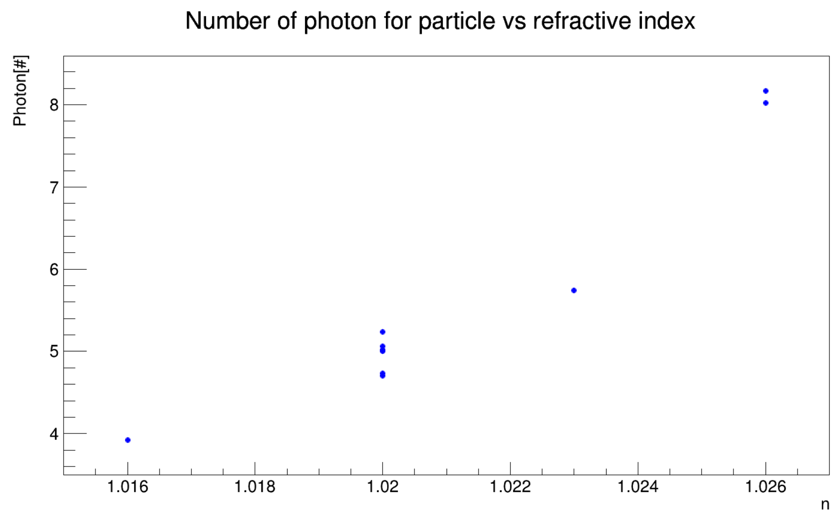

(a) The number of photons for particles detected by the prototype using aerogel with different refractive indices. The cluster of measurement at $n = 1.020$ is due to the fact that several tiles with this refractive index were tested, and the result from the 2022 test beam was also included.

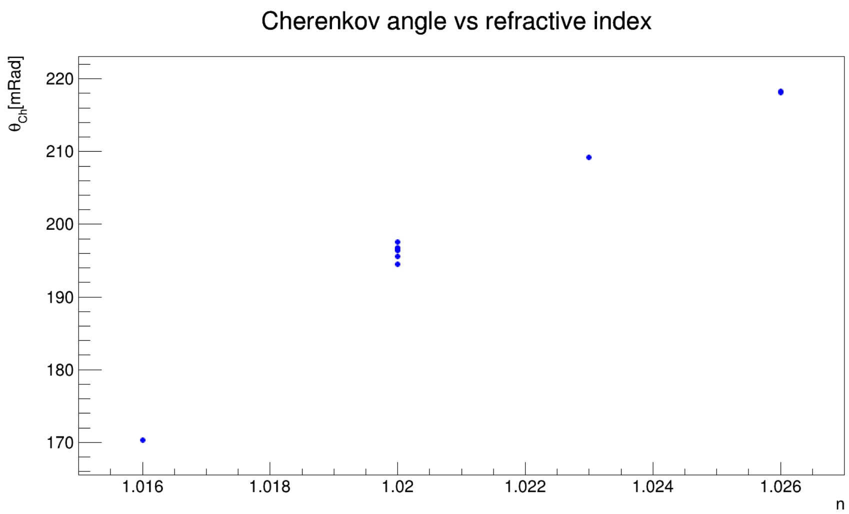

(b) Cherenkov angle measured by the prototype using aerogel with different refractive index. The cluster of measurement at $n = 1.020$ is due to the fact that several tiles with this refractive index were tested, and the result from the 2022 test beam was also included.

Figure 4.41: Results of 2023 aerogel study

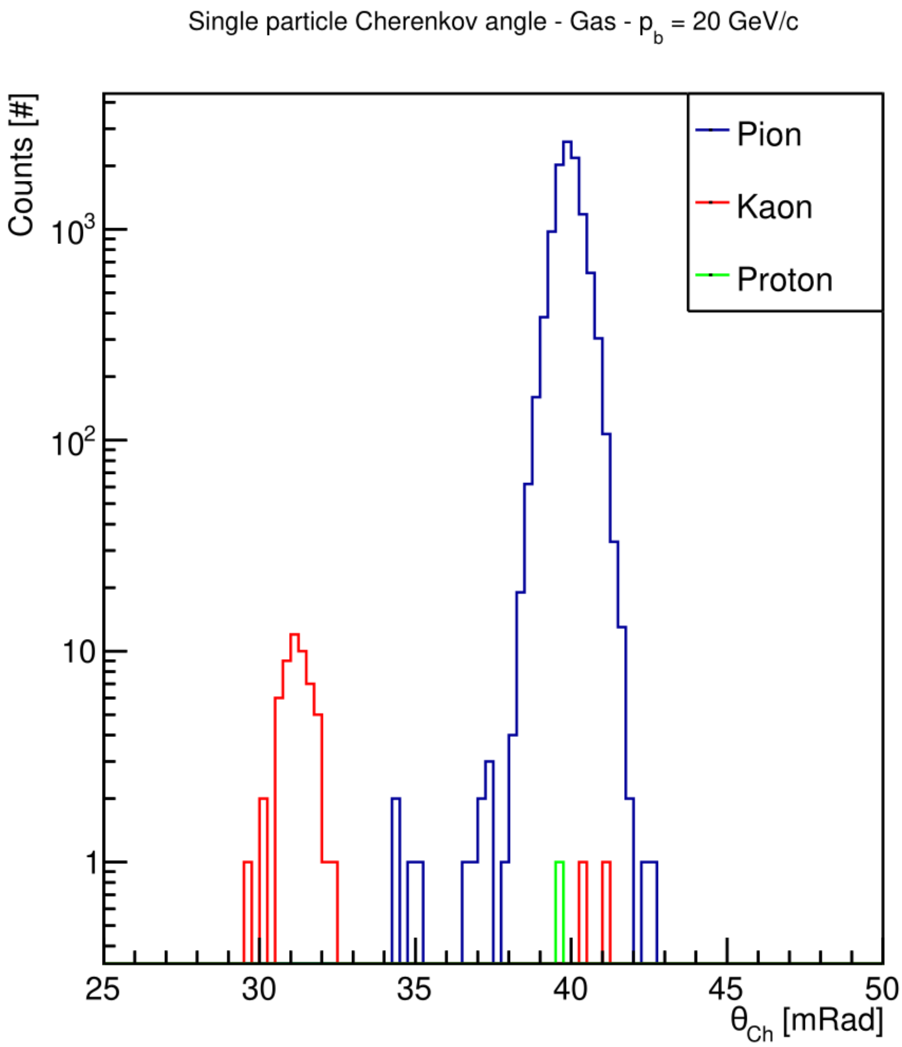

Figure 4.42: Distribution of the single-particle Cherenkov angle for gas photons, for particle species tagged by the beam PID system. At 20 GeV beam momentum, the kaon peak is clearly separated from the pion peak, while the proton does not produce a ring being below the Cherenkov threshold.

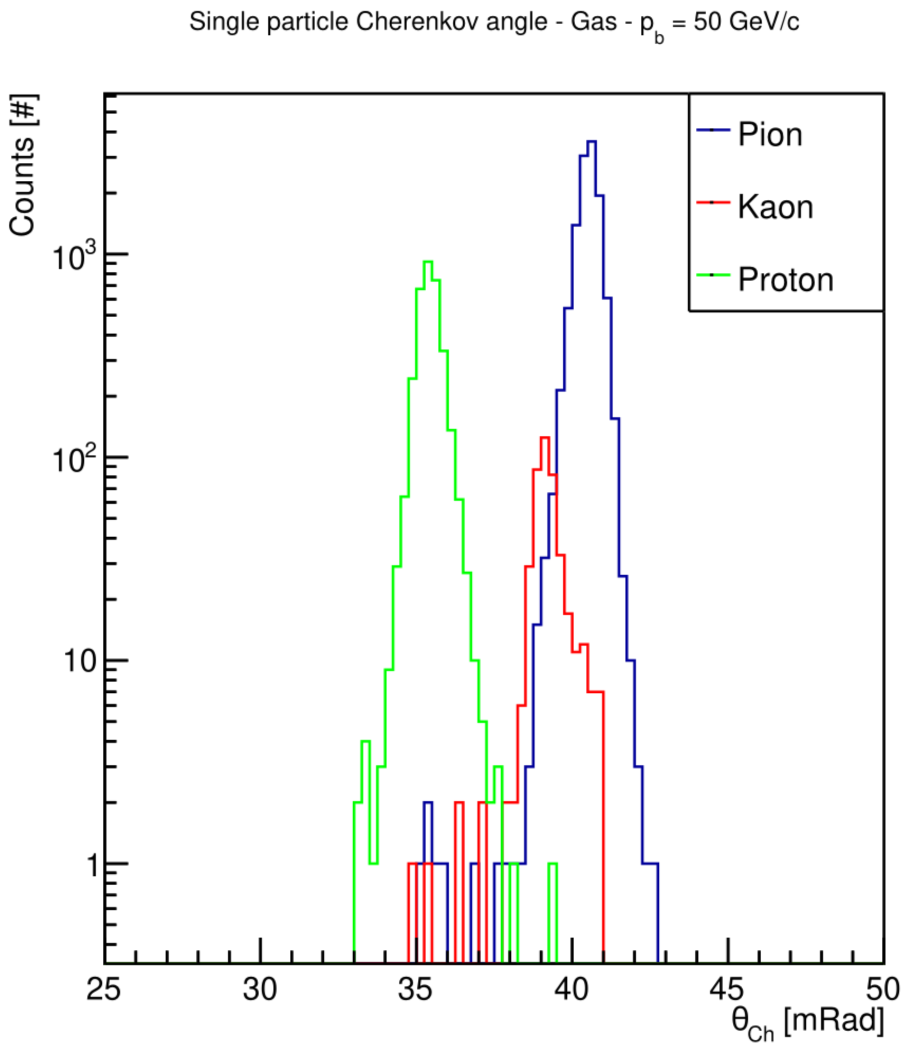

Figure 4.43: Distribution of the single-particle Cherenkov angle for gas photons, for particle species tagged by the beam PID system. At 50 GeV beam momentum, the kaon peak starts merging into the pion peak, while the proton peak is well separated from the others.

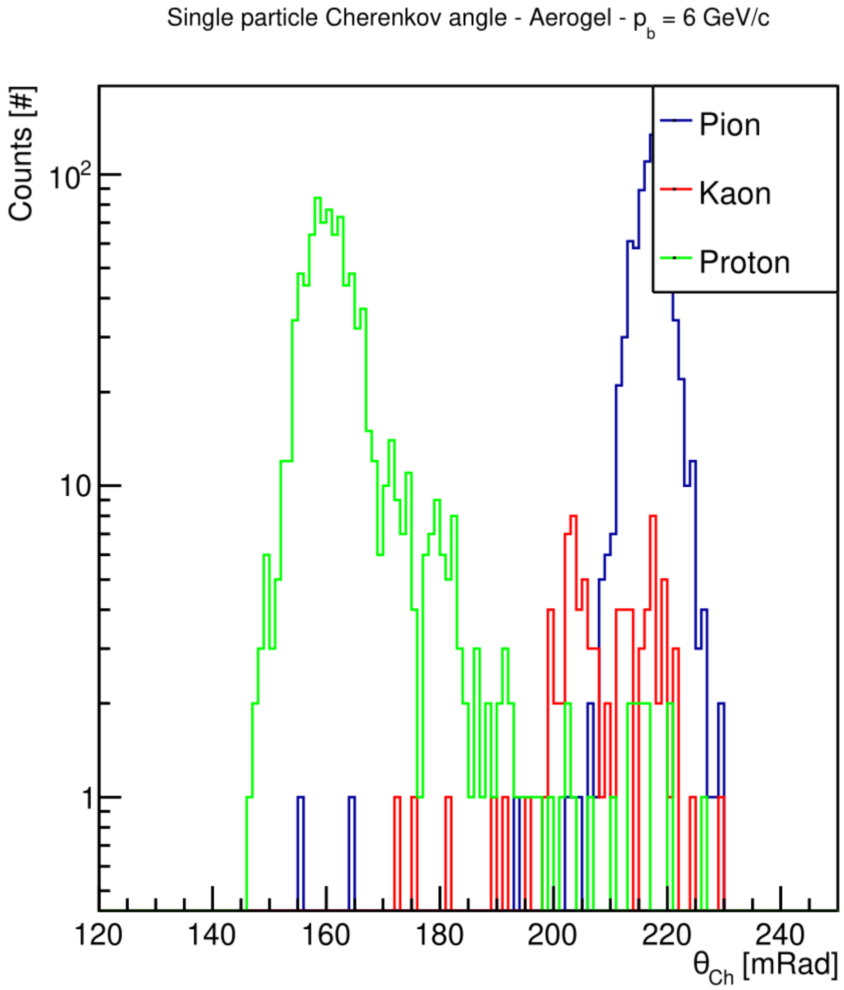

Figure 4.44: Distribution of the single-particle Cherenkov angle for aerogel photons, for particle species tagged by the beam PID system. At 6 GeV beam momentum, the proton peak is well separated from the others. The kaon peak is barely visible around 205 mRad, ~~although it is~~ diluted by the beam PID inefficiency.

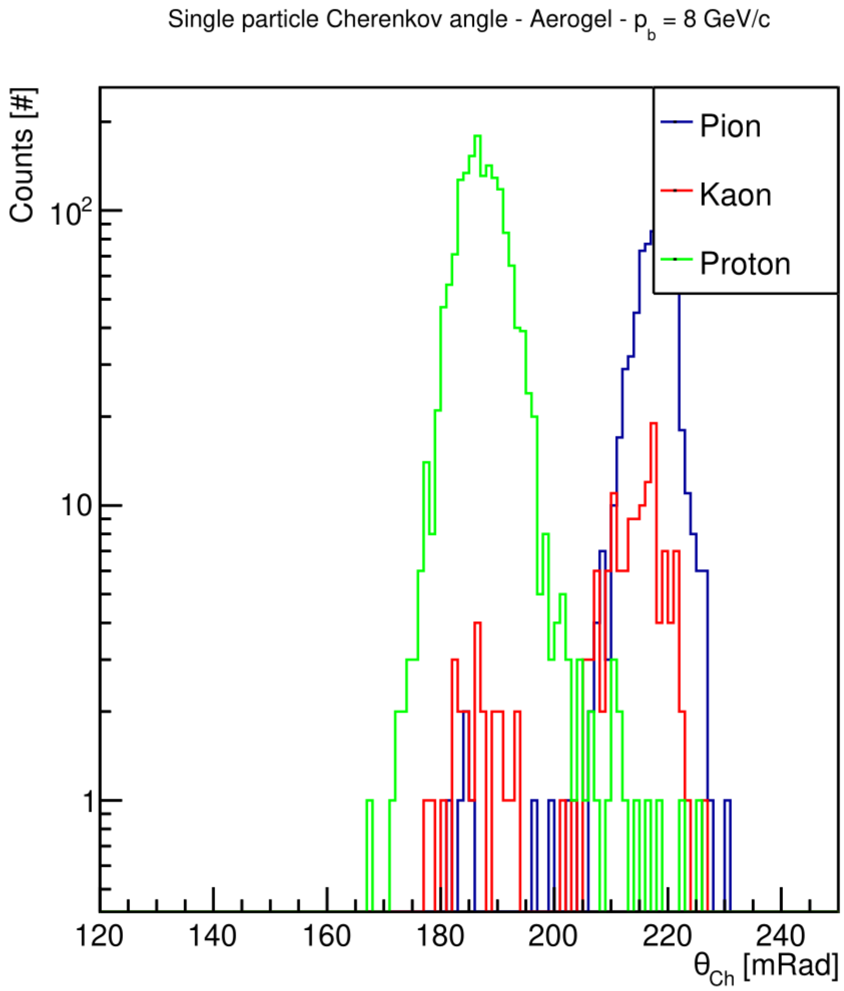

Figure 4.45: Distribution of the single-particle Cherenkov for aerogel photons, for particle species tagged by the beam PID system. At 8 GeV beam momentum, the proton peak is well separated from the others. Although the kaon peak is visible, it starts merging into the pion peak.

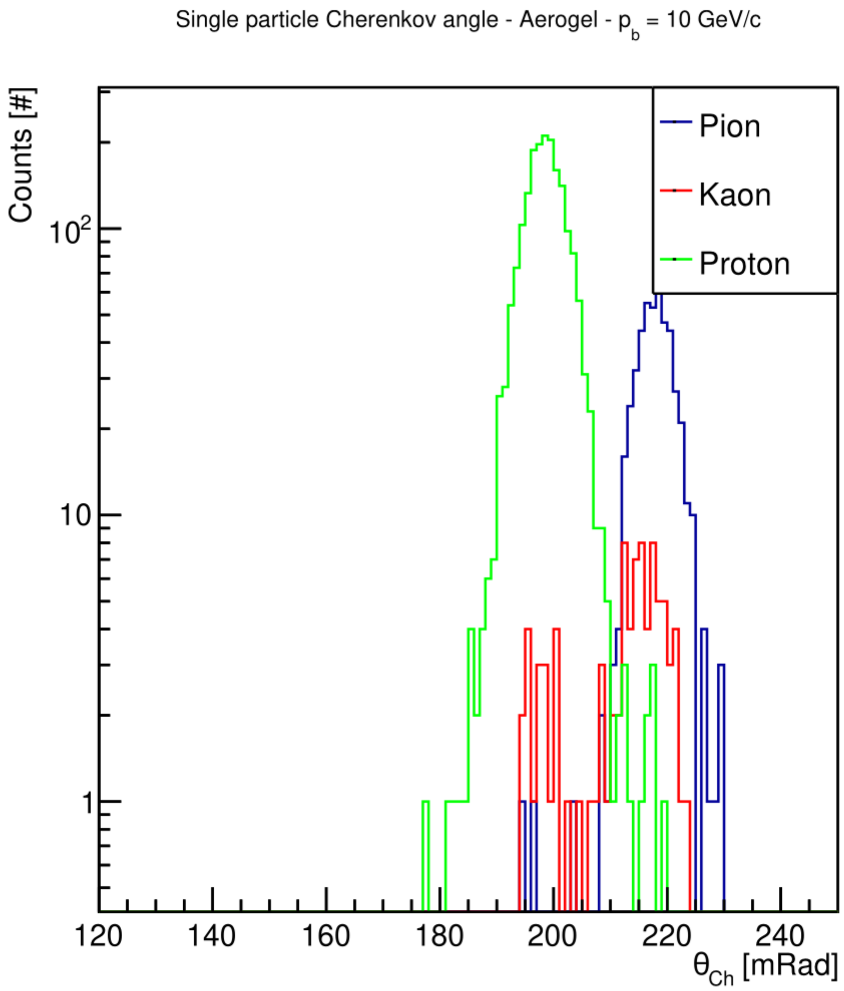

Figure 4.46: Distribution of the single-particle Cherenkov angle for aerogel photons, for particle species tagged by the beam PID system. At 10 GeV beam momentum, the proton peak is well separated from the others. The kaon peak results overlapping the pion peak.

by studying SIDIS reactions, which requires the detection of at least one hadron in the final state. The particle identification in the hadronic endcap of the ePIC experiment will be carried out by a dual-radiator Ring Imaging Cherenkov detector. The dRICH is being designed by a collaboration of several institutions led by ~~the~~ INFN ~~Ferrara division~~. This detector is facing two main challenges: the broad momentum range in which the hadron must be identified, and single-photon detection in high magnetic field. The moderate background radiation level expected at ePIC will damage the selected magnetic-insensitive ~~photosensors SiPMs~~. A study on recovering the photo-detectors via high-temperature annealing provided good indications, suggesting the possibility of performing the cure directly in-situ without removing the SiPMs.

A dRICH prototype was realized and tested between 2020 and 2023 to support the detector design phase. It allowed ~~us to test the MAPMTs data acquisition and~~ to measure the optical performance using a reference photon detector. The double rings were detected using the SiPM, and the SPE resolution measured for gas and aerogel is similar to the values expected from the simulation. These results support the design and the feasibility of the ~~ePIC detector~~, and will be further validated with a new real-scale prototype.